remote sensing

MDPI

Article

Characterizing the Distribution Pattern and a Physically Based Susceptibility Assessment of Shallow Landslides Triggered by the 2019 Heavy Rainfall Event in Longchuan County, Guangdong Province, China

Siyuan Ma [1,2], Xiaoyi Shao [3,4] and Chong Xu [3,4,*]

1 Institute of Geology, China Earthquake Administration, Beijing 100029, China
2 Key Laboratory of Seismic and Volcanic Hazards, Institute of Geology, China Earthquake Administration, Beijing 100029, China
3 National Institute of Natural Hazards, Ministry of Emergency Management of China, Beijing 100085, China
4 Key Laboratory of Compound and Chained Natural Hazards Dynamics, Ministry of Emergency Management of China, Beijing 100085, China
* Correspondence: chongxu@ninhm.ac.cn

Abstract: Rainfall-induced landslides pose a significant threat to the lives and property of residents in the southeast mountainous and hilly area; hence, characterizing the distribution pattern and effective susceptibility mapping for rainfall-induced landslides are regarded as important and necessary measures to remediate the damage and loss resulting from landslides. From 10 June 2019 to 13 June 2019, continuous heavy rainfall occurred in Longchuan County, Guangdong Province; this event triggered extensive landslide disasters in the villages of Longchuan County. Based on high-resolution satellite images, a landslide inventory of the affected area was compiled, comprising a total of 667 rainfall-induced landslides over an area of 108 km^2. These landslides consisted of a large number of shallow landslides with a few flowslides, rockfalls, and debris flows, and the majority of them occurred in Mibei and Yanhua villages. The inventory was used to analyze the distribution pattern of the landslides and their relationship with topographical, geological, and hydrological factors. The results showed that landslide abundance was closely related to slope angle, TWI, and road density. The landslide area density (LAD) increased with the increase in the above three influencing factors and was described by an exponential or linear relationship. In addition, southeast and south aspect hillslopes were more prone to collapse than the northwest –north aspect ones because of the influence of the summer southeast monsoon. A new open-source tool named MAT.TRIGRS(V1.0) was adopted to establish the landslide susceptibility map in landslide abundance areas and to back-analyze the response of the rainfall process to the change in landslide stability. The prediction results were roughly consistent with the actual landslide distribution, and most areas with high susceptibility were located on both sides of the river valley; that is, the areas with relatively steep slopes. The slope stability changes in different periods revealed that the onset of heavy rain on 10 June 2019 was the main triggering factor of these group-occurring landslides, and the subsequent rainfall with low intensity had little impact on slope stability.

Keywords: heavy rainfall; shallow landslides; TRIGRS model; spatial distribution; susceptibility assessment; Longchuan County; Guangdong Province

check for updates

Citation: Ma, S.; Shao, X.; Xu, C. Characterizing the Distribution Pattern and a Physically Based Susceptibility Assessment of Shallow Landslides Triggered by the 2019 Heavy Rainfall Event in Longchuan County, Guangdong Province, China. *Remote Sens.* **2022**, *14*, 4257. https://doi.org/10.3390/rs14174257

Academic Editors: Paolo Mazzanti and Saverio Romeo

Received: 29 July 2022
Accepted: 24 August 2022
Published: 29 August 2022

1. Introduction

In recent years, an increasing number of intense rainfall events have occurred in mountainous areas due to the impact of global climate change, which has dramatically increased the frequency of global rainfall-induced landslides [1,2]. Rainfall-induced landslides are not only widely distributed in the world but also occur frequently and cause significant damage to humanity [3–6]. Therefore, a good understanding of the fundamentals of rainfall-induced landslide occurrence, distribution patterns, and susceptibility assessments can provide useful guidance for regional disaster prevention and mitigation, and landscape evolution [7–9].

A new landslide inventory that is generated after a major triggering event (e.g., an earthquake, volcanic eruptions, or heavy rainfall) is referred to as an event-based landslide inventory. Owing to the advancements in earth observation technology, such as multi-temporal high-resolution optical satellite remote sensing, more high-quality earthquake-induced landslide inventories have been developed. In particular, since the 2008 Wenchuan earthquake, the establishment of coseisimic landslide inventories has made great progress. At present, there are roughly 46 detailed coseismic landslide databases mapped as polygons [10–13]. However, unlike earthquake events, the construction speed of landslide inventories triggered by heavy rainfall events is still relatively slow, and currently there are only a few heavy rainfall-induced landslide inventories [14–16]. The main reason is that clouds are often a major obstacle in the affected areas, which may limit the visibility of satellite images and thus affect the visual interpretation of rainfall-induced landslides [15]. At present, there are 16 public landslide inventories triggered by heavy rainfall events around the world, with the majority of these landslide databases being on a small scale. The southeast coastal region in China is economically developed and densely populated. Influenced by monsoon rainfall, this area is also considered a landslide-prone zone [17,18]. Once landslides occur, the social and economic losses in this area will be huge. A comprehensive rainfall-induced landslide database not only contributes to a deeper understanding of the event occurrence but also provides data support for the subsequent in-depth analysis of the formation and evolution of the geological disaster chain[15,19]. However, there are few rainfall-induced landslide inventories for a single event in the southeast coastal region, and thus more analyses are needed for rainfall-induced landslide inventories in this area.

Rainfall-induced landslide susceptibility can provide valuable information for landslide risk assessment. Currently, there are two quantitative methods for assessing the susceptibility for rainfall-induced landslides, which include the data-driven methods based on mathematical methods and physical-based methods that couple the hydrological models and infinite slope stability models. For the data-driven method, the relationship between the influencing factors and the landslide occurrence are analyzed by mathematical models [20–22]. Currently, many models have been widely used in landslide susceptibility mapping, particularly with the development of machine learning technology, such as logistic regression [23,24], random forest [25], artificial neural network [26], convolutional neural network (CNN) [27], support vector machine (SVM) [28], and decision tree [29]. However, the outcomes of landslide susceptibility mapping based on the data-driven method could be subject to considerable uncertainties due to errors and variability in model choice, data selection, system understanding of weighting factors, and human judgment [30,31]. Meanwhile, the data-driven model does not possess the timeliness of emergency assessment for a single triggering event, because it requires sufficient landslide data to establish the susceptibility assessment model. As a consequence, assessment results frequently lag behind practical application and cannot serve the emergency assessment in a short time [32,33]. Otherwise, due to the fact that the majority of these models are trained by regional landslide data and are thus limited by regional geological and geomorphic characteristics [14,34,35], the data-driven model's applicability in different areas is greatly diminished. However, the physically based landslide susceptibility assessment can better solve the above problems.

Unlike the data-driven method, the physically based method does not take into account actual landslide data, but rather simulates the physical process of rainfall-induced landslide occurrence by coupling the hydrological and infinite slope models [36]. The physically based method has been pervasively used because of its high predictive capability and the most acknowledged feasibility for a quantitative assessment of the effects of the individual parameters that contribute to landslide initiation [37] and it is a useful tool for determining the susceptibility zonation of rainfall-induced shallow landslides [38].

In addition, the wide application of GIS technology facilitates the wide application of physical models in large areas [39,40]. Due to its preferable practicability and wide regional applicability, physically based models are popular in the spatial prediction of regional rainfall-induced landslides [41–45]. In recent years, some physically based models for rainfall-induced landslide susceptibility mapping have been developed, such as the TRIGRS model [40], the Slip model [46–48], the GIS-TiVaSS model [45,49], the GIS-TISSA model [50], the CRESTSLIDE model [51,52], and the HIRESSS model [53–55]. Among them, the TRIGRS model, which accounts for transient pore water pressure, can predict the impact of heavy rainfall on groundwater changes in a short period. At present, it is the most widely used physically-based model of slope instability [41,56–58], and has been used in many countries around the world, including Italy, the United States, China, South Korea, and Southeast Asia [59–64]. However, the application of the TRIGRS model in China's southeast area is limited so it is necessary to investigate the applicability of the model in the spatio-temporal prediction of rainfall-induced landslides in the southeast mountainous area.

Longchuan County experienced continuous heavy rainfall from 10 June 2019 to 13 June 2019. Extensive landslides, collapses, and debris flows occurred in the villages of Longchuan county. A total of 352 villages of Longchuan County were devastated to varied degrees, of which Mibei village in Beiling town was the most severely hit with 1571 individuals affected, 120 buildings fully collapsed, and more than 100 houses damaged. The direct economic loss of this event reached CNY 110 million, exerting a significant impact on the normal productivity and lives of local residents. Thus, the objectives of this study are: (1) establishing a landslide inventory including landslides induced by the 2019 Longchuan heavy rainfall event and analyzing the spatial distribution of landslides with topographical, geological, and hydrological factors; (2) conducting the physically based susceptibility assessment based on a new open-source tool named MAT.TRIGRS(V1.0) for predicting the spatiotemporal distribution of rainfall-induced landslides and back-analyzing the response of the rainfall process on the change of landslide stability.

2. Study Area

Longchuan County is situated in the northeast of Guangdong Province, spanning from 23.8°N to 24.7°N of latitude and from 115.0° to 115.6°E of longitude, and covers an area of approximately 3089 km^2 on the surface. The study area is Beiling Town, which is located in the north of Longchuan County and the upper reaches of Dongjiang River. The climate in the region is subtropical monsoon with abundant rainfall and sunshine. The annual rainfall is 1500 mm, and the average temperature is about 22 °C. The study area experiences the most rainfall in May, June, and July. The geomorphic unit of the study area is a hilly landform with an elevation range from 100 m to 1100 m (Figure 1). The mountains are steep, and the peaks are conical due to the relatively developed hydrographic nets and strong topographic cutting in this area. As a result, numerous "V" shaped valleys developed in this area, with slope angles ranging from 20 to 50 degrees. The main lithology of the study area is acid intrusive rock of Ordovician and Silurian, mainly monzogranite (O_3-S_1), which accounts for more than 70% of the rock in the whole study area (Figure 2a). In addition, tuff of Yousheng formation of Middle Cretaceous (K_{2ys}) and quartz mica schist of Daganshan formation of Sinian(Z_{2djs}) also developed in this area (Figure 2a). The main land use type is forest, which accounts for 80% of the whole study area, followed by cropland, accounting for more than 10% (Figure 2b).

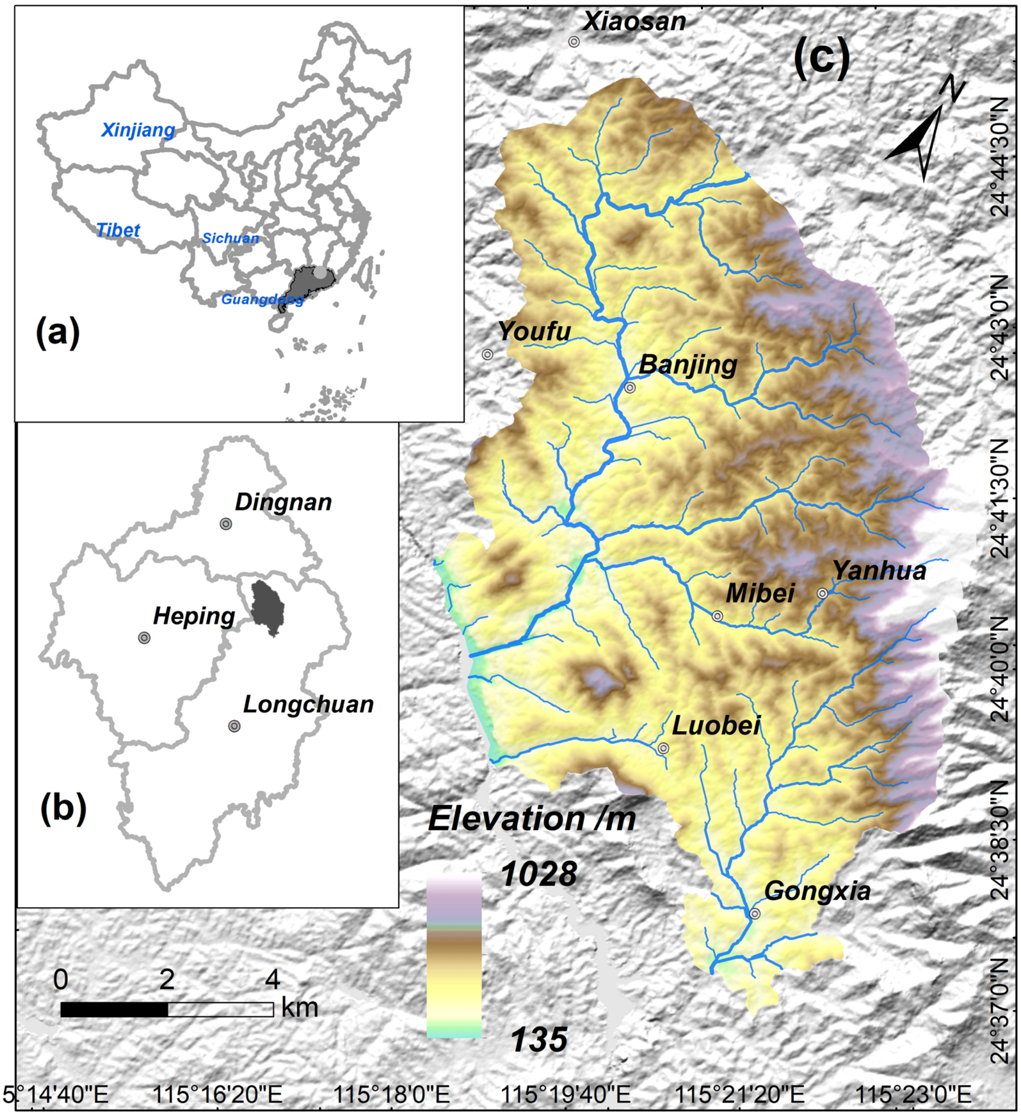

Figure 1. Mapping shows the location and elevation of the study area; (**a**) Guangdong Province; (**b**) location of Longchuan county; (**c**) the elevation and water net distribution of the study area.

Due to the unique geographical and climatic conditions, Longchuan area experiences several large or small rainstorms every year, making it one of most vulnerable zones to geological disasters. From 10 June 2019 to 13 June 2019, Longchuan County suffered continuous heavy rainfall; this rainfall event triggered a large number of landslides. As far as local people can recollect, since the evening of the 10 June 2019, transportation has been disrupted, communication has been lost, and electricity has been cut off. Meanwhile, the settlement below the mountain was engulfed in mist, and the sound of collapses and landslides was constant.

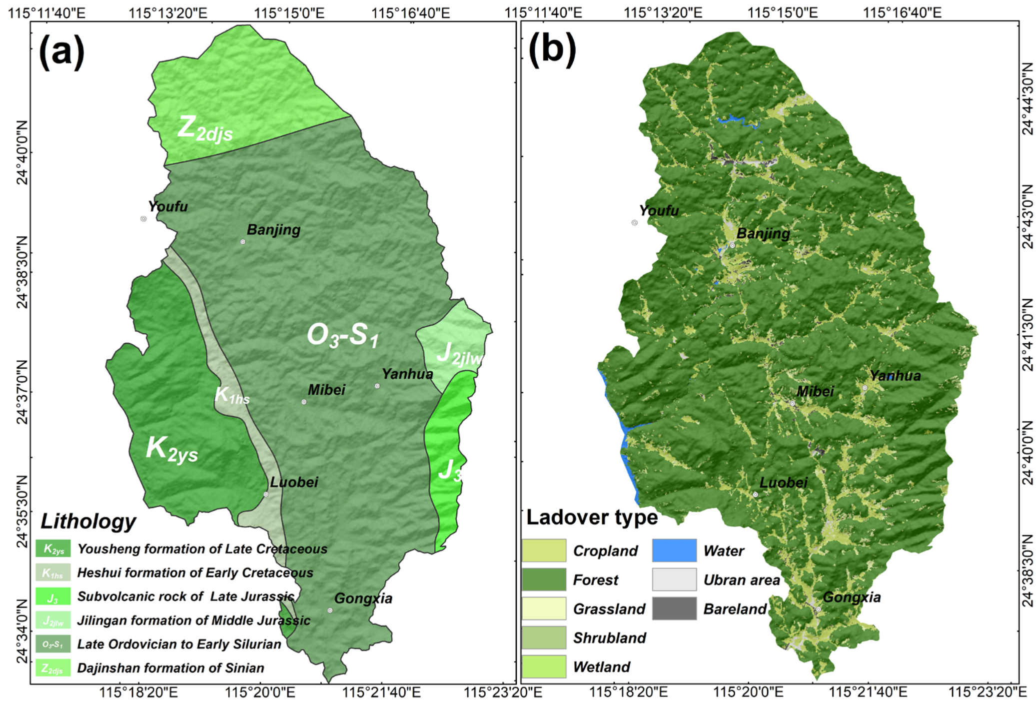

Figure 2. (**a**) Geological map of the study area obtained from 1:200,000 geological maps published by China Geological Survey (http://dcc.cgs.gov.cn/, accessed on 1 July 2022); (**b**) the land use type map of the study area derived from the 10-m resolution global land cover results [65].

3. Data and Method

3.1. Landslide Mapping

The availability of high-resolution satellite images on the Google Earth (GE) platform allowed us to conduct a detailed visual interpretation of landslides [66,67]. The remote sensing images used for landslide interpretation in this study are based on the GE platform. It was important that the high-resolution satellite image covered the entire study area, and the dates of images before and after the rainfall event were mainly in January 2019 and January 2021. Meanwhile, given the relatively long interval between the images before and after the rainfall event, we obtained the Sentinel-2 images with 10 m resolution as a supplementary (the pre- and post-events images were 17 April 2019 and 24 September 2019, respectively) (Figure 3). The landslide inventory was checked by Sentinel-2 images to ensure that the interpreted landslides were caused by the 2019 rainfall event. The reason for selecting these two images was that they had the closest interval between rainfall events without cloud cover in the study area. Landslides were identified by visual interpretation and mapped as polygons. Since the study area has high vegetation coverage, landslides can be better delineated by satellite images before and after this event. Figure 3 depicts the Sentinel-2 satellite images before and after the rainfall. According to remote sensing images, most landslides triggered by this event were small and medium-scale shallow landslides, and a majority of them were located near Mibei village, showing obvious group-occurring characteristics (Figure 4).

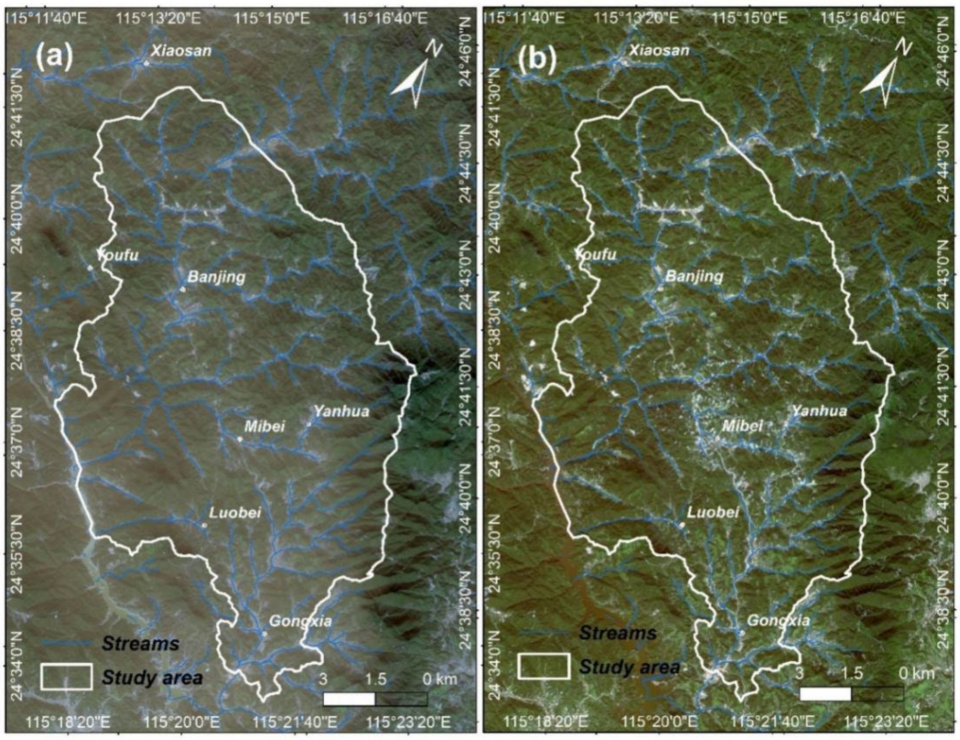

Figure 3. Mapping shows the Sentinel-2 images before and after the rainfall event; (**a**) satellite image before rainfall event taken on 17 April 2019; (**b**) satellite image before rainfall event taken on 24 September 2019.

Figure 4. (**a**) Aerial photograph of Mibei village after the rainfall event, houses are damaged by rainfall-induced landslides; (**b**) group-occurring shallow landslides; (**c**) the landslide damaged the hillside residences, and the floors on the second floor crashed on the first floor; (**d**) road damage caused by landslides (Picture source: http://www.gdlctv.com/Pc/index/new_detalis.html?id=3320, accessed on 25 June 2022).

3.2. Rainfall Data

We collected the precipitation data over the past two decades from 2000 to 2020 in Longchuan County (Figure 5). The results show that the average rainfall remained between 1200 and 2400 mm, with periodic fluctuations. The annual rainfall in 2006 and 2017 was unusually high, reaching almost 2300 mm or more. In comparison, the annual rainfall in 2019 was low with 1500 mm, which was roughly the same as the recent 20-year average (Figure 5a). Comparing the monthly rainfall in 2019 with the average value over the past two decades (Figure 5b), we also found that the rainfall from March to June in 2019 was higher than the monthly average rainfall in the last 20 years. The precipitation in June of 2019 was 300 mm, slightly higher than the monthly average rainfall of 250 mm in previous years.

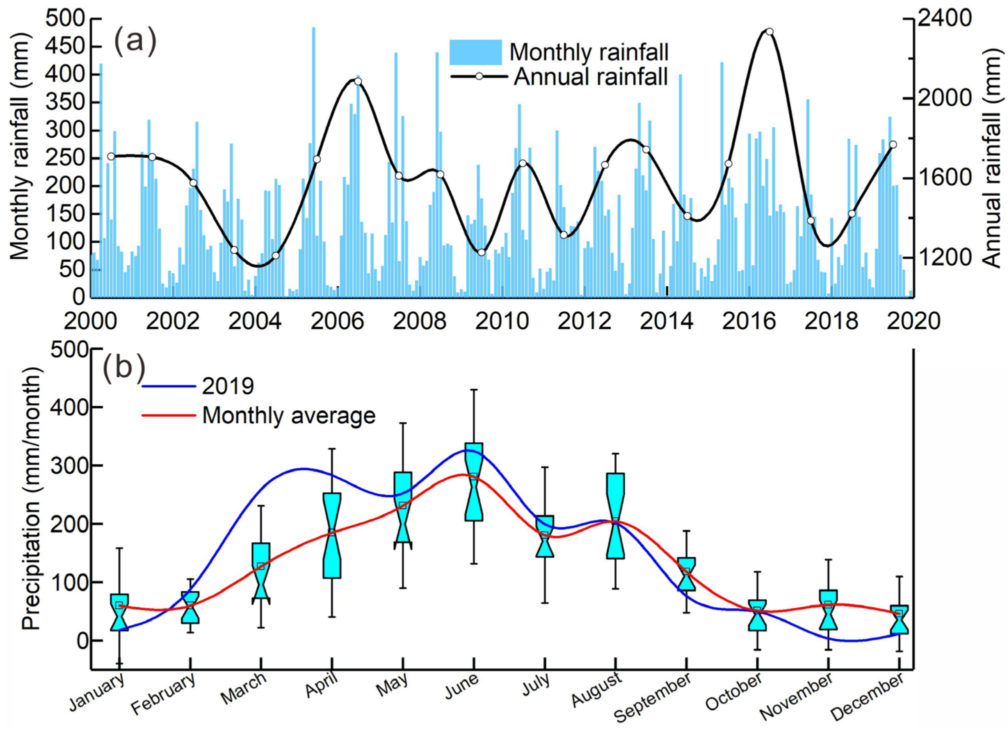

Figure 5. Monthly rainfall data of Longchuan County in the past 20 years from 2000 to 2020; (**a**) monthly and annual average rainfall data over the last 20 years; (**b**) comparing the monthly rainfall in 2019 with the average value over the last two decades.

We obtained the data for the rainfall every 12 h based on the rainfall stations of China Meteorological Administration. Eight national rainfall stations within 50 km of the study area were utilized for interpolation, and the most popular Kriging interpolation algorithm was used to obtain the spatial distribution of rainfall (Figure 6). The results show that this rainfall event occurred primarily from 10 June 2019 to 13 June 2019 (Figure 7). The cumulative rainfall was basically the same, remaining at 210 to 220 mm, with rainfall in the west slightly higher than that in the east (Figure 6). Figure 8 shows the distribution of daily rainfall from 10th to 13th of June during this rainfall event. The rainfall on 10 June 2019 was the heaviest, peaking at around 120 mm, accounting for more than half of this rainfall event. The rainfall for the next three days was expected to be around 20–40 mm. Otherwise, the spatial change of daily rainfall in the study area from June 10 to 13 was relatively small, and the difference of daily rainfall of the study area was essentially maintained within 10 mm.

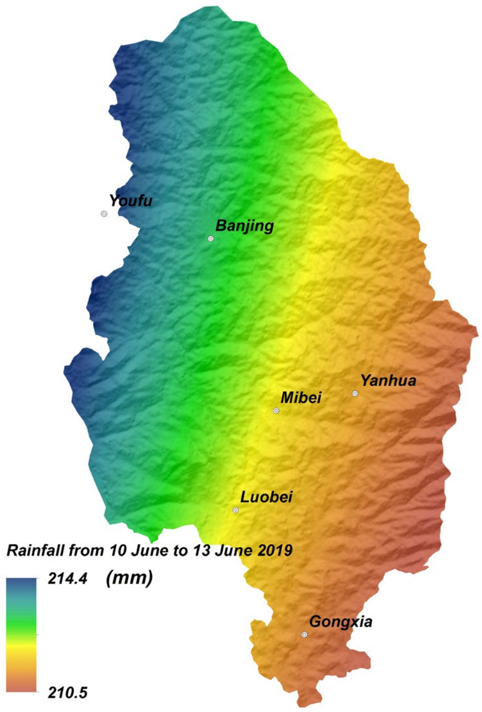

Figure 6. Mapping shows the spatial distribution of total rainfall from 10 June 2019 to 13 June 2019.

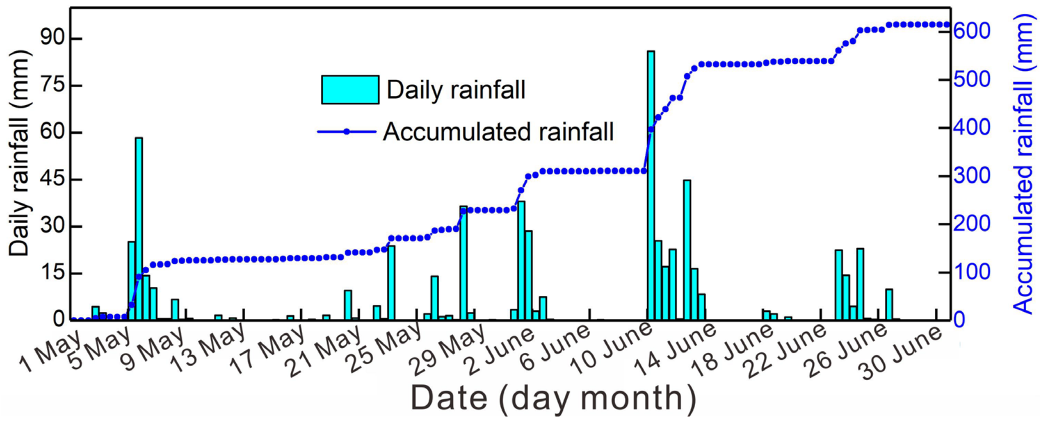

Figure 7. Data of the rainfall every 12 h from the national rainfall stations in the study area from 1 May to 30 June.

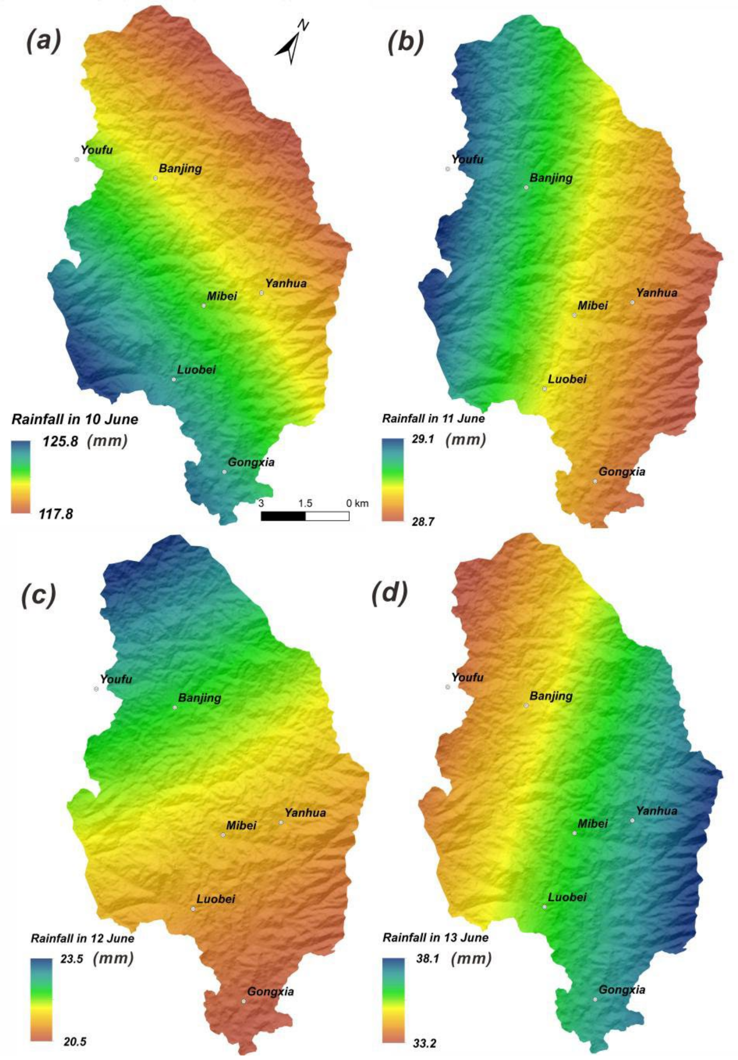

Figure 8. Mapping shows the distribution of daily rainfall from the 10th to 13th of June during this rainfall event; (**a**) 10 June 2019; (**b**) 11 June 2019; (**c**) 12 June 2019; (**d**) 13 June 2019.

3.3. Data Related to Other Influencing Factors

To assess the role of topographic, geologic, and hydrologic factors on the distribution of rainfall-induced landslides, we obtained several terrain metrics (i.e., elevation, hillslope gradient, and topographic relief) and lithologic and hydrological data. The elevation data were derived from ALOS PALSAR DEM with 12.5 m resolution, which were then resampled into a 5 m resolution based on the bilinear algorithm. The hillslope gradient and slope aspect were derived from the DEM data. In addition, we estimated the topographic relief from the elevation range within a 1.0 km radius. TWI was computed using GRASS GIS and the DEM data. Drainages were also derived from DEM by AcrGIS. The road data were downloaded from the OpenStreetMap Data (https://master.apis.dev.openstreetmap.org/export#map=11/35.2510/103.4308, accessed on 5 June 2022). The lithology data are obtained from 1:200,000 geological maps published by China Geological Survey (http://dcc.cgs.gov.cn/, accessed on 1 July 2022). The land use type data were derived from the 10 m resolution global land cover results [65]. The spatial distribution of the above influencing factors was converted into a raster format with a grid cell size of 5 m. Finally, seven influencing factors were considered for the statistical analysis, including the elevation, hillslope gradient, relief, slope aspect, land use type, road density, and distance to river (Figure 9). Meanwhile, the relationship between different influencing factors and the occurrence of landslides were analyzed by the polygon feature.

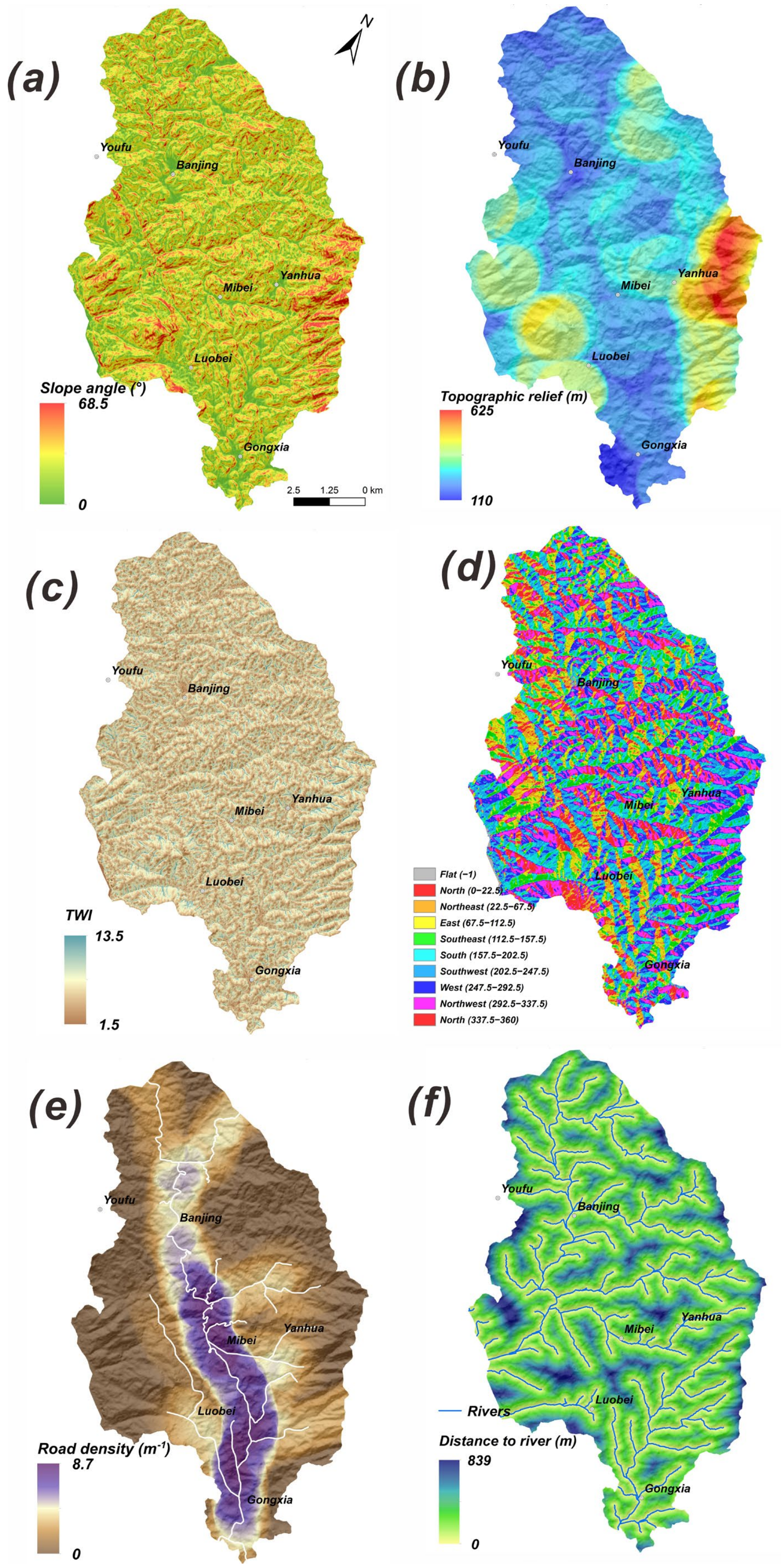

Figure 9. Mapping showing the distribution of the influencing factors in the study area; (**a**) slope angle; (**b**) topographic relief; (**c**) topographic wetness index; (**d**) aspect; (**e**) road density; (**f**) distance to river.

3.4. TRIGRS Model

The TRIGRS model (Transient rainfall infiltration and grid-based regional slope-stability model) is a widely used and effective evaluation model of rainfall-induced shallow landslide susceptibility [68,69]; the model was developed by the United States Geological Survey (USGS) [40,70] and written by Baum et al in FORTRAN [40], and it needs specific input parameters, mainly including rainfall parameters, soil mechanics parameters, and hydrological parameters of the study area. Following the determination of the parameters, the grid stability caused by the change of transient pore water pressure of each grid during the rainfall period is calculated based on the GIS platform for the purpose of evaluating the slope stability of all grids in a certain rainfall period.

Iverson [36] linearized the solution of the Richards equation and this serves as the foundation for the infiltration models for wet initial conditions. It consists of a steady component and a transient component of seepage. The steady seepage is determined by the initial depth of the water table and steady infiltration rate. Under steady infiltration, the slope is stable. Transient infiltration is the short-term change in pore water pressure caused by rainfall. The infinite slope model is then applied using the computed transient pore water pressure. The generalized solution in TRIGRS is:

$$\begin{gathered}\psi(Z,t) = (Z-d)\beta + 2\sum_{n=1}^{N} \frac{I_{nz}}{K_s} H(t-t_n)[D_1(t-t_n)]^{\frac{1}{2}} \\ \sum_{m=1}^{\infty}\left\{ ierfc\left[\frac{(2m-1)d_{LZ}-(d_{LZ}-Z)}{2[D_1(t-t_n)]^{\frac{1}{2}}}\right] + ierfc\left[\frac{(2m-1)d_{LZ}+(d_{LZ}-Z)}{2[D_1(t-t_n)]^{\frac{1}{2}}}\right]\right\} - \\ 2\sum_{n=1}^{N} \frac{I_{nz}}{K_s} H(t-t_{n+1})[D_1(t-t_{n+1})]^{\frac{1}{2}} \sum_{m=1}^{\infty}\left\{ ierfc\left[\frac{(2m-1)d_{LZ}-(d_{LZ}-Z)}{2[D_1(t-t_{n+1})]^{\frac{1}{2}}}\right] + ierfc\left[\frac{(2m-1)d_{LZ}+(d_{LZ}-Z)}{2[D_1(t-t_{n+1})]^{\frac{1}{2}}}\right]\right\}\end{gathered} \tag{1}$$

where ψ is the groundwater pressure head; t is time; N is the total number of time intervals; Z is depth below the ground surface in the vertical coordinate direction; d is the depth of steady-state water table; d_{LZ} is the depth of the impermeable basal boundary; $\beta = \cos^2\delta - (I_{ZLT}/K_s)$, δ is the slope angle; I_{ZLT} is the steady surface flux; Ks is the saturated hydraulic conductivity; I_{nZ} is the the surface flux or rainfall intensity for the nth time interval; $D_1 = D_0/\cos^2\delta$, D_0 is the saturated hydraulic diffusivity; and $H(t-t_n)$ is the Heaviside step function in which t_n is the time at the nth time interval in the rainfall infiltration sequence.

$$ierfc(\eta) = \frac{1}{\sqrt{\pi}}\exp\left(-\eta^2\right) - \eta erfc(\eta) \tag{2}$$

where $erfc(\eta)$ is the complementary error function.

The model calculates infiltration (I) at each cell as the sum of precipitation (P) and any runoff from upslope cells (Ru), with the caveat that infiltration cannot exceed the saturated hydraulic conductivity (Ks):

$$I = P + R_u,\ if\ P + R_u \le K_s \tag{3}$$

$$I = K_s,\ if\ P + R_u > K_s \tag{4}$$

When $P + Ru$ exceeds Ks in a cell, the excess is considered runoff (Rd) and is diverted to nearby downslope cells.

$$R_d = P + R_u - K_s,\ if\ P + R_u - K_s \ge 0 \tag{5}$$

$$R_d = 0,\ if\ P + R_u - K_s < 0 \tag{6}$$

The TRIGRS model calculates the slope stability using an infinite-slope stability analysis (Equation (7)), as described in Iverson [36]. The ratio of resistant basal coulomb friction to gravitationally induced downslope basal driving stress characterizes the instability of an infinite slope in the failure analysis [71]. This ratio F_s, is computed at depth Z by

$$F_s(Z,t) = \frac{\tan\varphi'}{\tan\delta} + \frac{c' - \psi(Z,t)\gamma_w \tan\varphi'}{\gamma_s Z \sin\delta\cos\delta} \quad (7)$$

where c' is the cohesion of the soil, φ' is the friction angle, γ_s is the unit weight, and γ_w is unit weight of groundwater.

The flow chart of this study is shown in Figure 10.

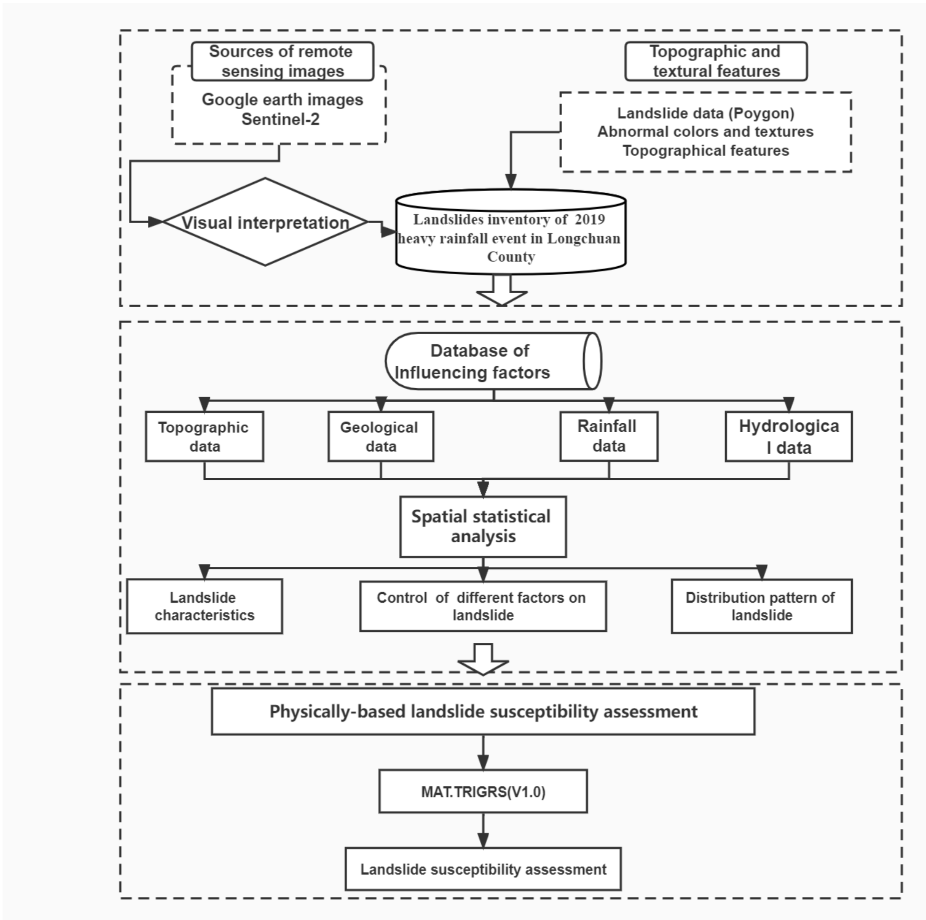

Figure 10. Flow chart of this study.

4. Rainfall-Induced Landslide Inventory

4.1. Basic Characteristics

This rainfall event triggered 667 landslides over an area of 108 km^2, and the majority of them (552 landslides) occurred in the Mibei and Yanhua villages (Figure 11a,b). The types of landslides were various, including shallow landslides combined with a small number of flowslides, rockfalls, and debris flows with a total landslide area of 0.75 km^2. The largest landslide area was approximately 20,000 m^2, the smallest area was 50 m^2, and the average landslide area was about 1100 m^2. According to the statistics, there were 288 landslides with an area of less than 500 m^2, accounting for approximately 43% of all landslides. There were 291 landslides with an area of 500~2000 m^2, accounting for approximately 44%. The number of landslides with an area of 2000~5000 m^2 and > 5000 m^2 was 71 and 17, respectively (Figure 10).

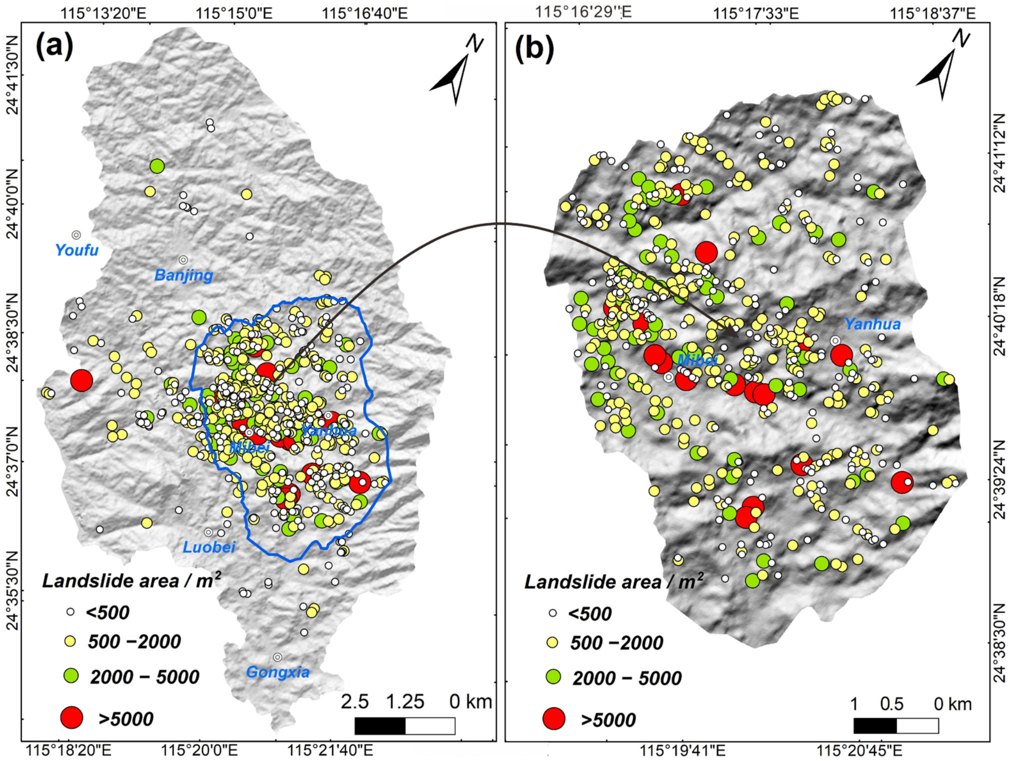

Figure 11. (**a**) Rainfall-induced landslide inventory of the 2019 heavy rainfall event in Longchuan County, the landslide abundance area of this event; (**b**) map showing the zooming of the landslide abundance area.

We calculated the landslide number density (LND) and landslide area density (LAD) within a 1.5 km-radius moving window using a Gaussian density kernel function. The LND and LAD maps indicated that the maximum LAD and LND of the study area were 9.5% and 78/km^2, respectively (Figure 11). Landslides had obvious cluster distribution characteristics, and a large number of landslides were concentrated within 2 km of the Mibei Village (Figure 12).

4.2. Factor Analysis

In order to analyze the relationship between different influencing factors and the occurrence of landslides, we calculated the frequency distribution of landslides and landscape (i.e., non-landslide area) and the LAD of different influencing factors. Figure 13 shows the frequency density distribution of landslide and non-landslide areas, and Figure 14 shows the LAD in different intervals of six influencing factors (the higher the LAD, the more likely the landsliding will occur). For elevation, the frequency density distribution of landslide area and non-landslide area was basically the same (Figure 13a), the peak LAD was situated at elevations from 300 to 450 m, indicating that landslides were more likely to occur within this elevation range (Figure 14a). For the slope angle, the landscape area was clustered between 5 and 20°, while most of the landslides occurred on slopes with the inclination of 15–35° (Figure 13b). Overall, the LAD increased with the increase in the slope angle and was described by an exponential relationship of $y = e^{(0.21+0.08x)}$, (where x is the slope angle and y is the LAD, Figure 14b), suggesting that with the increase in the slope angle, the landslide occurrence possibility also increased. In terms of topographic relief, the relief of non-landslide area was primarily concentrated in the 200~250 m range, whereas the landslide area was primarily clustered in the range of 250~350 m (Figure 13c). Overall, there was a negative logarithmic relationship between the LAD and relief, indicating that the LAD decreased with the increase in relief (Figure 14c). On the part of TWI, landslides were most commonly seen in the range with TWI values between

4 and 6, and there was a positive exponential relationship between the LAD and TWI of $y = e^{(-12.16+1.18x)}$ (where x is the TWI and y is the LAD), and the LAD increased as the TWI increased (Figure 14d). For road density, landslides were primarily distributed in the road density interval between 2 and 4 (Figure 13d). In general, LAD and road density had a linear relationship of $y = 0.14x + 0.45$ (where x is the road density and y is the LAD), which shows that landslides were more likely to occur in areas with a high road density (Figure 14e). For the distance to river, landslides were more likely to occur in the range of 100~400 m, and there was no obvious correlation between the LAD and the river distance (Figure 14f).

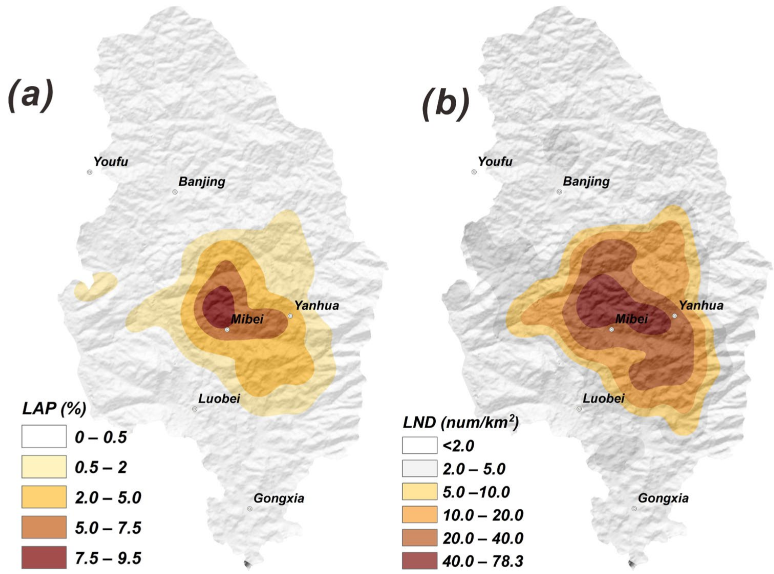

Figure 12. Map showing spatial density of landslides triggered by this rainfall event. (**a**) landslide number density (LND); (**b**); landslide areal density (LAD).

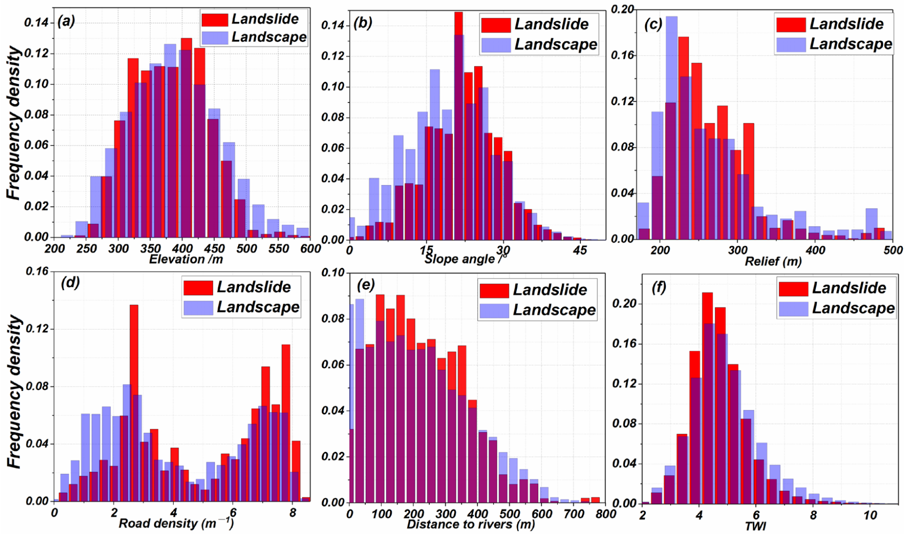

Figure 13. Frequency density estimates of landslides and landscape area for different influencing factors; (**a**) slope angle; (**b**) elevation; (**c**) relief; (**d**) road density; (**e**) distance to rivers; (**f**) TWI.

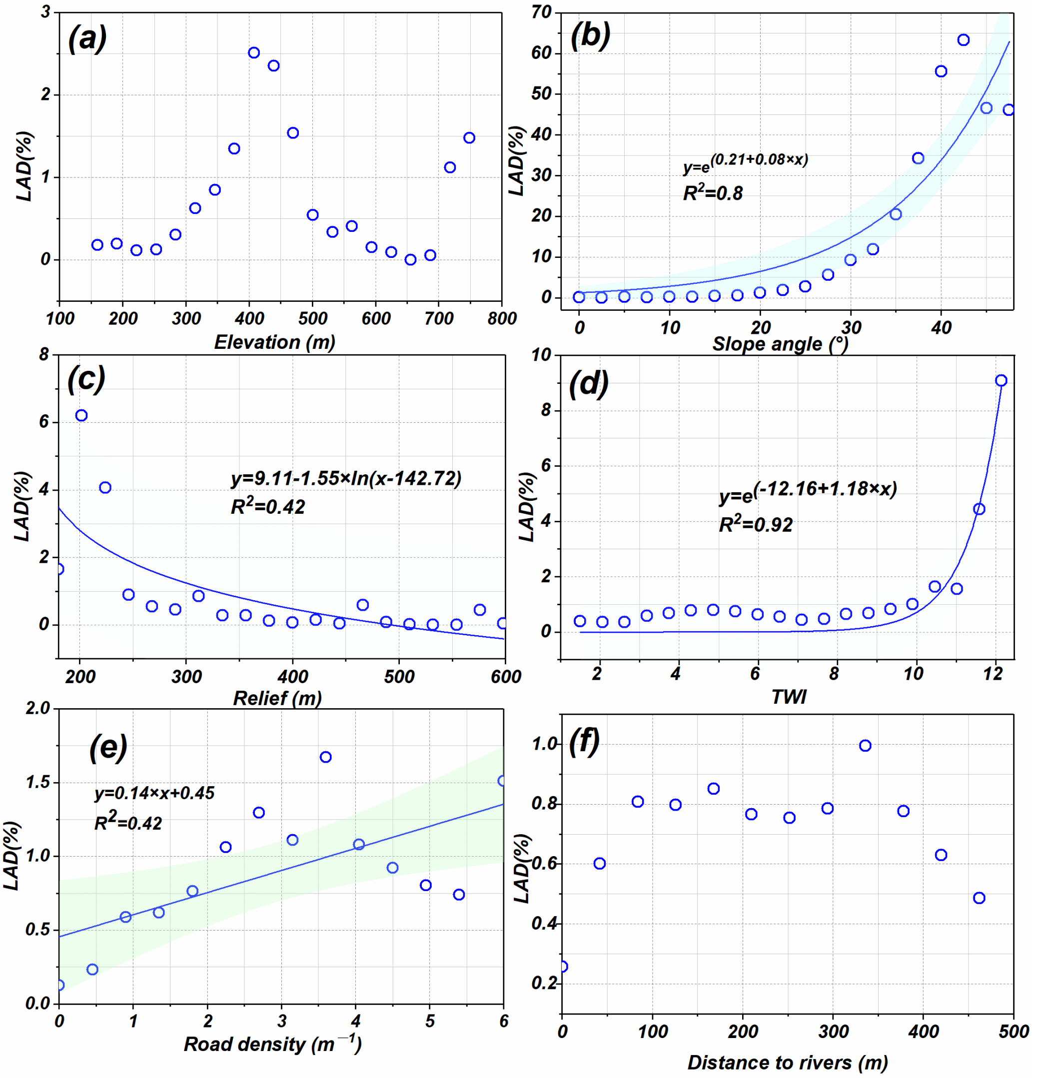

Figure 14. Map showing the relationship between the six influencing factors and the landslide areal density (LAD); (**a**) elevation; (**b**) slope angle; (**c**) topographic relief; (**d**) TWI; (**e**) road density; (**f**) distance to rivers.

Figure 15 shows the statistical results of the landslides and the slope aspect. Figure 15a shows the frequency density of the landslides and landscape (i.e., non-landslide area) on different slope aspects. The result demonstrates that the non-landslide area was evenly distributed in all aspects, but most of the landslide area was concentrated in the aspect of 110°~180° (SE to S). The statistical results of LAD show that the peak LAD of 1.4% was present at the aspects from SE to S for the landslides.

Figure 16 shows the distribution of the landslide and non-landslide area, and the average landslide area in each land use unit. The result shows that the predominant land type was forest, which accounts for 80% of the study area, followed by cropland land, which accounts for more than 10%. The area of urban area and bare land was less than 1%. Among all land types, shrubland was the most prone to landslides, with roughly 10% of landslides occurring in the 5% area. Landslides were the least developed in cropland, maybe due to the relatively gentle slope of this unit. Furthermore, statistics on the average landslide area of different units suggest that bare land had the largest average landslide area, with more than 1600 m^2, followed by forest land, which had an average landslide area of 1200 m^2, and cropland had a relatively small average landslide area, only 600 m^2.

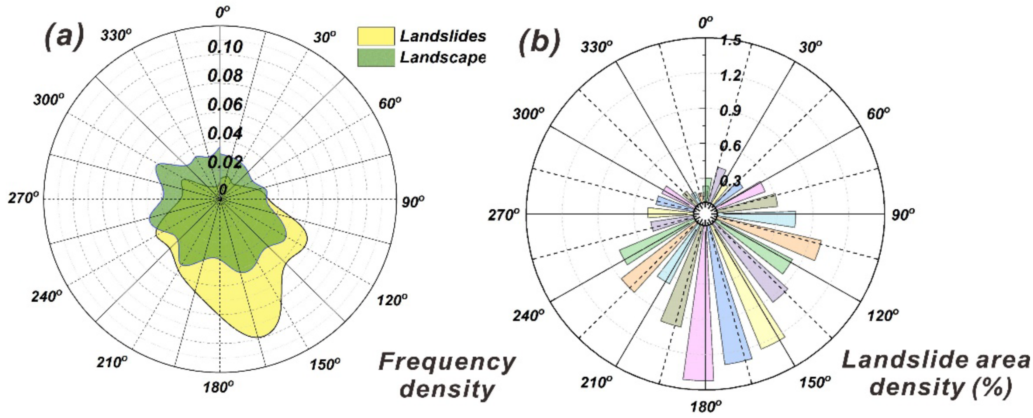

Figure 15. (**a**) The distribution of aspect within landslides and landscape; (**b**) correlations between aspect and landslide area density (LAD).

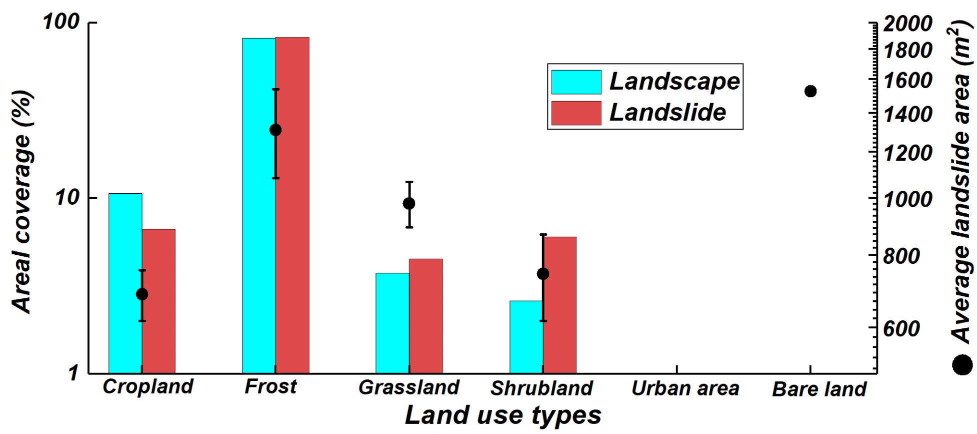

Figure 16. Areal coverage (%) of different land use types for both landslide and landscape overlaid by average landslide area calculated per each unit.

5. Physically Based Landslide Susceptibility Assessment

5.1. Brief Description of MAT.TRIGRS(V1.0)

To address the issues of the manual modification of plentiful model parameters and complex data processing in the traditional TRIGRS model, Ma, et al. [72] proposed a new TRIGRS model using Matlab®programming. It can directly read the grid data of TIF format as the input, and then directly exports the prediction results of grid files, which greatly simplifies data preparation and parameter setting. It includes the script files INPUT DATA.m and TRIGRS.m. The INPUT DATA.m file is used to read the TIF input files, and TRIGRS.m is the executable program that can be used to calculate the pressure head and Fs. The minimum Fs and the corresponding pressure head are generated in the TIF format by calculating the pressure head and Fs at various soil depths. More description can be obtained in [72].

In the physically based model, in order to obtain accurate landslide prediction results, sufficient and accurate input data are required [68,73–75]. For the soil thickness distribution, the Z-model developed by Saulnier, et al. [76] was used to evaluate the soil thickness. We assumed that the maximum thickness of the soil in the study area was 5 m and the minimum thickness was 0.5 m based on previous studies [17,77]. Soil thickness can be estimated and calculated by Equation (8). The bedrock in the study area is monzogranite (O_3-S_1), and the landslide occurred primarily in the weathered soil layer on the bedrock's surface. The soil type of the weathered soil layer is sandy clay loam. Therefore, combined with previous studies [17,52,78], we assigned the corresponding values to mechanical and hydrological parameters including cohesion, internal friction angle, and soil weight of this soil type (Figure 17 and Table 1). Based on previous experience [57,79], saturated hydraulic diffusivity D0 was set to $D_0 = 200K_s$ and the initial surface flux (I_{ZLT}) was generally less than the Ks to one power or more and was set to $I_{ZLT} = 0.01K_s$.

$$h_i = h_{max} - \left(\frac{Z_i - Z_{min}}{Z_{max} - Z_{min}}\right)(h_{max} - h_{min}) \quad (8)$$

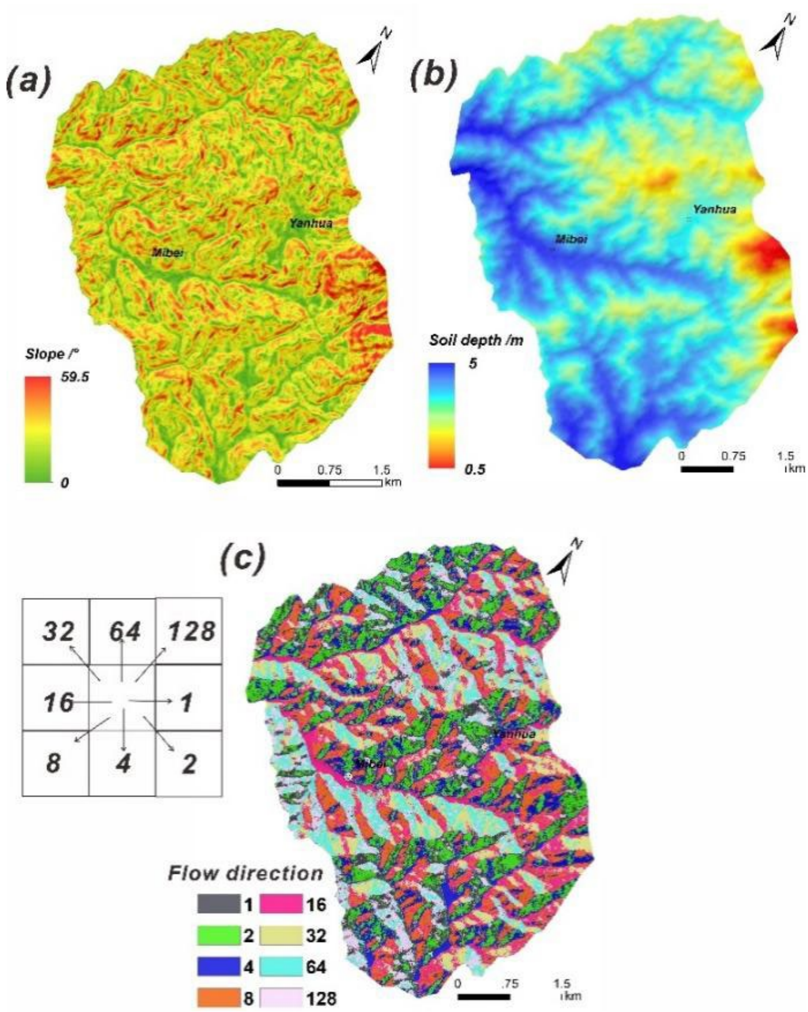

Figure 17. Maps showing the distribution of slope angle (**a**), soil thickness (**b**) and flow direction (**c**).

Table 1. Mechanical properties of the soil.

Input Parameters	Cohesion (Kpa)	Friction Angle (°)	Unit Weight (kN/m^3)	Saturated Hydraulic Conductivity (m/s)
	29	20	15	6.59×10^{-6}

Simultaneously, in order to account for the uncertainties in the physical process that lead to slope failure, the Monte Carlo simulation, which is a robust and well-known approach in applications concerning probability analyses and reliability studies, was used in this study [56,80]. We considered the uncertainties of two main parameters (cohesion and internal friction angle) that primarily influence the slope failure. To characterize the probability density function (PDF) of the two random variables, the normal PDF was adopted. We assumed that the average and standard deviation of the cohesion were 29 kPa and 9 kPa and those of the internal friction angle were 20° and 6°. Based on the Monte Carlo simulation, the input data were calculated by the TRIGRS model, yielding 1000 predicted pictures of potential landslides in the study area. Finally, the slope failure probability (Pf) of the study area was obtained.

5.2. Landslide Susceptibility Assessment

Figure 18 shows the distribution of the average value of 1000 predicted pictures calculated by rainfall data over different time periods. From the calculation results, we can observe that the Fs of all raster cells were greater than that before the rainfall event, indicating that all slopes were stable (Figure 17a). In addition, after 12 h of the rainfall (at 8:00 on 10 June 2019) 12-h rainfall reached 86 mm), the Fs of some grid cells in the study area decreased. Particularly, some grid cells with a large slope angle began to fail (Figure 17b). Then, although continuous rainfall occurred in the subsequent stage (after 11 June 2019), the change of Fs in the study area was relatively small, and few new grid units became unstable.

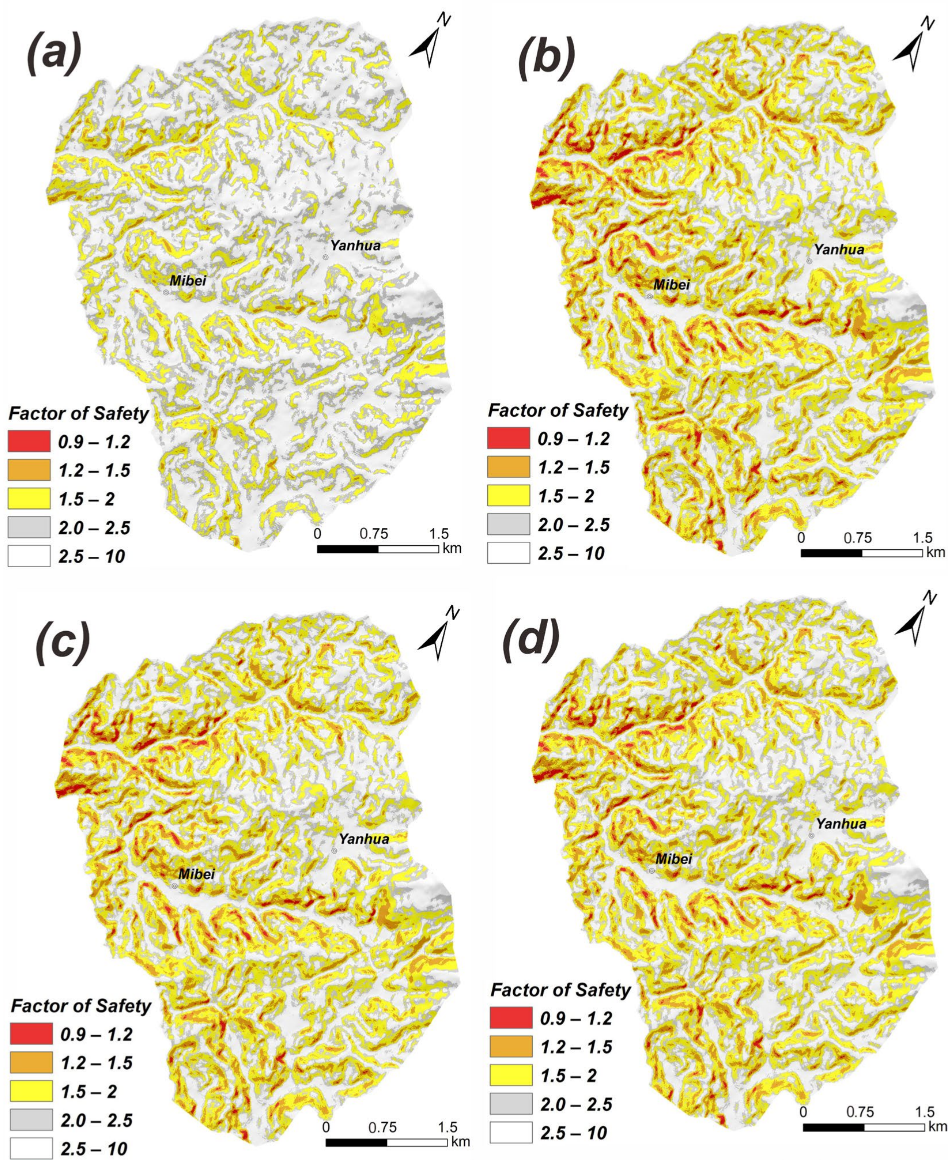

Figure 18. Slope stability conditions, expressed in terms of Safety of Factor (FS) in different time periods of this rainfall event; (**a**) 20:00 on 9 June 2019 (UTC + 8, before rainfall event); (**b**) 8:00 on 10 June 2019 (UTC + 8); (**c**) 20:00 on 11 June 2019(UTC + 8); (**d**) 8:00 on 13 June 2019(UTC + 8).

We calculated the Fs results in the various slope interval over different time periods (Figure 19). The result shows that the Fs of the grids with slope angles between 30 and 40° was mostly distributed between 1.3 and 2.5, with an average value of around 1.6. After the onset of heavy rain on 10 June 2019, the Fs of raster cells rapidly decreased, and the Fs of most grids ranged between 0.9 and 1.7, with an average value of about 1.2. From 8:00 on 10 June 2019, although there was rainfall every day at a subsequent stage, the average rainfall was less than 2 mm/h. The low rainfall intensity had a little impact on the slope stability. Rainfall increased to some extent on 12 June 2019, reaching 45 mm in 12 h, and the Fs decreased slightly. For grids with a slope larger than 40°, we also found the same trend that the Fs of most grid units decreased rapidly after heavy rainfall, and then basically remained unchanged. Overall, the Fs of grids with a slope greater than 40 degrees was much smaller than grids with a slope between 30 and 40 degrees.

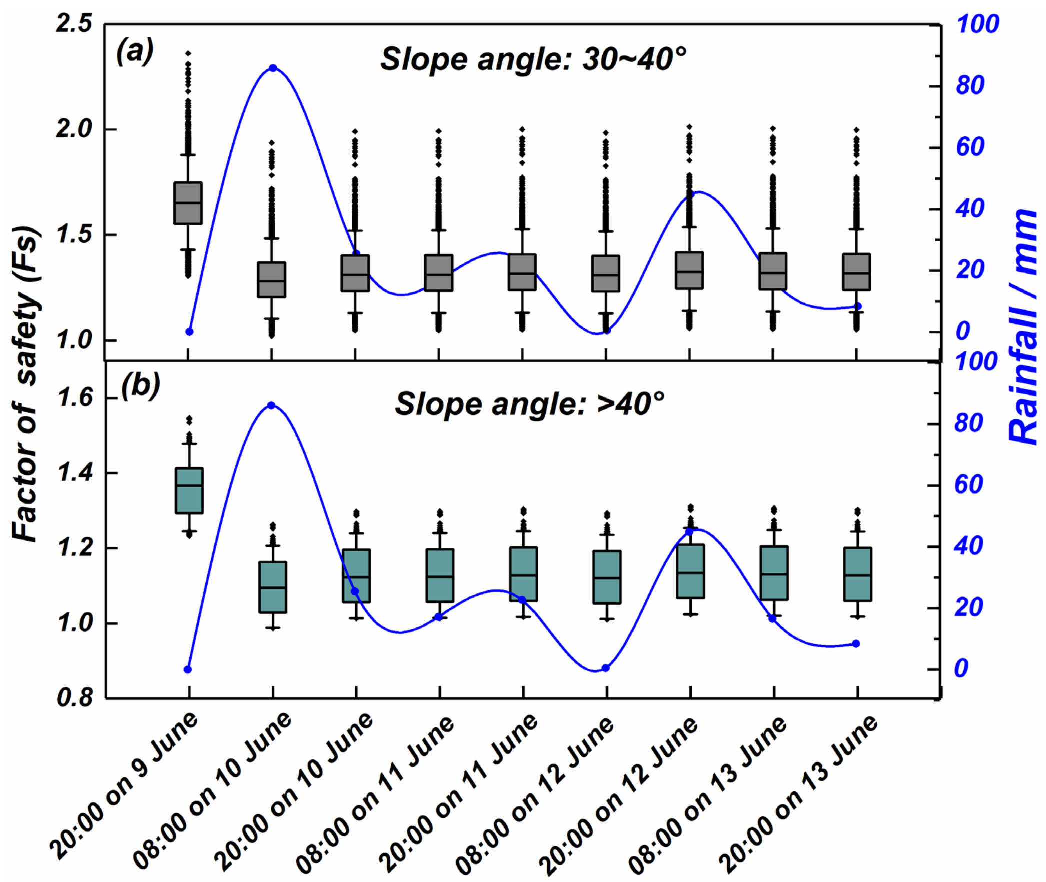

Figure 19. The statistical results of Factor of safety (Fs) in the various slope interval at different rainfall times; (**a**) slope angle: 30~40°; (**b**) slope angle: >40°.

Figure 20 shows the probability distribution of slope failure in different time periods. Obviously, the prediction results of Pf were roughly consistent with the actual landslide distribution. Most areas with a high probability (blue areas) were located on both sides of the river valley, that is, the areas with relatively steep slopes. Before rainfall, almost all the grids in the study area were less than 0.1, indicating that the slope before rainfall was stable. After 12 h of rainfall (at 8:00 on 10 June 2019), the area with steep slopes began to show the instability phenomenon, and the Pf of some grids reached more than 0.6. In the following continuous rainfall, with the decrease in rainfall intensity, there was a slight increase in the area with a high probability of failure.

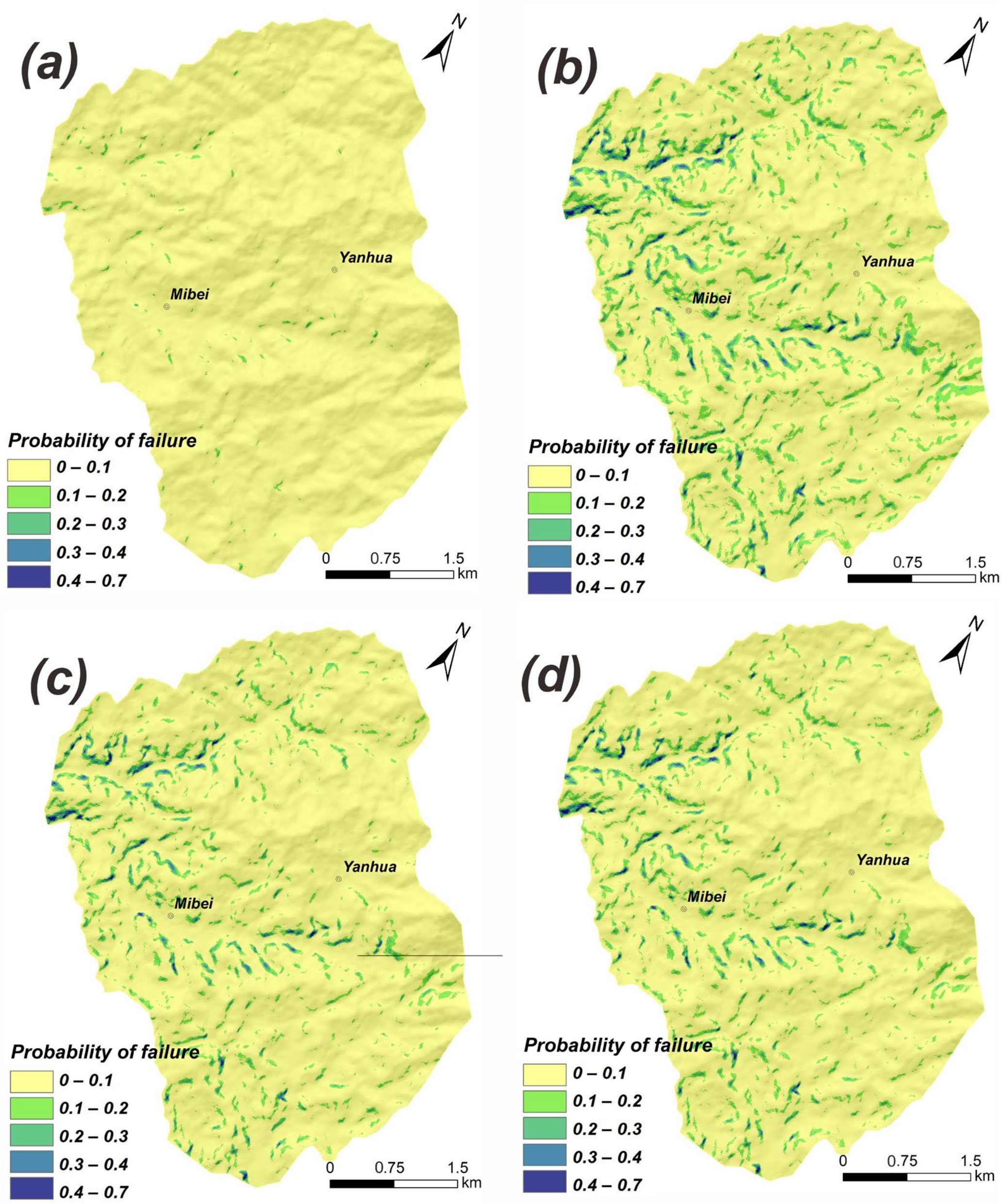

Figure 20. Probability of slope failure (Pf) in different time periods of this rainfall event; (**a**) before rainfall event; (**b**) 8:00 on 10 June 2019; (**c**) 20:00 on 11 June 2019; (**d**) 8:00 on 13 June 2019.

To quantitatively analyze the susceptibility results, we counted the class area, landslide area, and the corresponding LAD of different susceptibility classes before and after rainfall (Figure 21). Based on the natural breaks, the susceptibility level was divided into four classes (i.e., very low, low, moderate, and high). The result shows that before the occurrence of rainfall, most areas belonged to the low susceptibility area, and the majority of landslides were concentrated in very low and low susceptibility areas. With the occurrence of rainfall, the area of low susceptibility areas decreased, while the area of high susceptibility areas increased. The statistical result reveals that 12.1% of the total landslides occurred in the 25.0% of the area which were classified as moderate and high. Meanwhile, the LAD increased with the increase in the susceptibility level, which also shows that the model can effectively predict the potential landslide-prone zone.

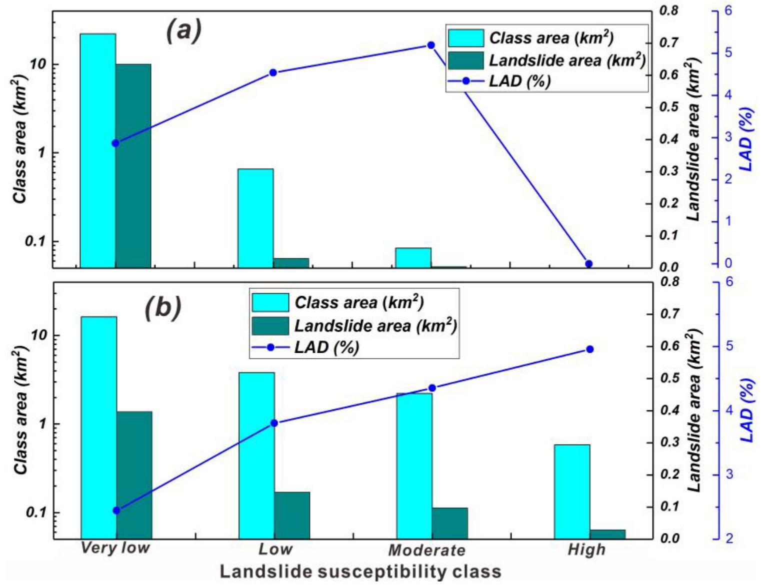

Figure 21. Susceptibility class distribution and the occurrence of landslides within the study area; (**a**) before rainfall; (**b**) after rainfall.

6. Discussion

China's southeast area is situated in a subtropical monsoon climate zone with frequent typhoons and rainstorms. The most common types of geological hazards in this area are landslides and debris flows caused by rainfall, which have the characteristics of a small scale of individual hazard point, a large number of groups, and a wide distribution range [18,19]. In mountainous areas, the effect of the orographic amplification of rainfall and the projection of rainfall-vector on hillslopes [81,82] might result in the windward hill-slope receiving more rainfall, leading to more landslides on the hillslope scale [83]. Due to the influence of the monsoon depression and tropical cyclone, the southeast monsoon prevails in the Longchuan area during the summer (June and July). The landslide distribution of this rainfall event indicates that the southeast and south aspect hillslopes are more prone to collapse than the northwest-north aspect ones (Figure 14). The main reason for this phenomenon is that the south slope is mostly windward, which causes more rainfall and splash erosion in the area. Otherwise, the bedrock weathering degree of the south slope will also be high due to the influence of environmental factors such as soil moisture content, surface temperature, light time, and so forth, leading to relatively weak mechanical parameters of rock and soil mass. Therefore, under the condition of heavy rainfall, the south slope is more prone to landsliding.

Slope angle is an important topographic factor affecting the occurrence of landslides. From the spatial distribution of the landslides, we can observe that the landslides were mainly distributed in low mountainous areas, with the sections at elevations within 300~450 m and slopes ranging from 15 to 35° (Figure 12). The LAD increased with the increase in slope angle and was described by an exponential relationship, indicating that the landslides of this event more easily occurred in areas with steep slopes (Figure 13b). TWI reflects how surface morphology affects soil groundwater level and moisture content, which is represented by a theoretical measure of the accumulation of flow [84,85]. According to the statistical results, there was an exponential relationship between the LAD and TWI, and the LAD increased as the TWI value increased. Especially when the TWI was greater than 10, the LAD increased rapidly (Figure 14f). Higher soil moisture causes higher pore water pressure and reduces the strength of rock and soil mass. As a result, when it rains, the pore water pressure in these areas rises rapidly, resulting in slope failure.

Anthropogenic factors (such as land-use change, deforestation, hill cutting, etc.) play a significant role in the initiation of landslides in active mountain ranges [86–88]. The construction of roads has significantly altered the slope stability of mountainous areas, making them prone to landslides. When a road is built, the toe of the slope is excavated or the weight of the slope is increased, and the overall stability above the slope is reduced, resulting in the occurrence of new landslides or the reactivation of old landslides[89]. From Figure 13d, we can observe that the landslides of this event were more likely to occur in areas with high road density, illustrating that anthropogenic factors have accelerated the instability of the slope in this area. Furthermore, in the Longchuan area, the majority of local residents have excavated mountains to build houses, leading to a number of nearly vertical artificial slopes. Meanwhile, human activities will fragment surrounding natural slopes and increase the degree of rock weathering, which will also exacerbate slope instability in mountain areas.

The formation lithology of the slope is the material basis of landslides. Granite layers are one of the most common strata in China's southeast coastal regions. Long-term weathering of granite results in widely distributed residual soil layers. For the Longchuan area, the bedrock is monzogranite (O_3-S_1), and the landslides occurred primarily in the weathered soil layer on the bedrock surface [17,77]. The major influence depth of heavy rainfall was limited to the superficial zone of slopes due to the difference in rainfall intensity and permeability of granite residual soil. This is why the shallow surface zone was severely affected by landslides [17]. A saturated seepage field was formed in the shallow surface zone of slopes as a result of prolonged heavy rainfall. The mechanical strength of saturated soil diminished, and slide failure occurred at the shallow surface saturation zone.

7. Conclusions

In this work, we established a landslide inventory including all the landslides induced by the 2019 Longchuan heavy rainfall event in Guangdong Province, China. We described the topographical, geological, and hydrological control of landslide hazards. Furthermore, we conducted the physically based susceptibility assessment of shallow landslides based on the MAT.TRIGRS (V1.0) tool. The following conclusions can be drawn: (1) This rainfall event triggered about 670 landslides with a total area of 0.75 km^2; the landslides had obvious cluster distribution characteristics, and a large number of landslides were concentrated within 2 km of the Mibei village. (2) The landslide abundance was closely related to slope angle, TWI, and road density but had a low correlation with elevation and distance to rivers. Among them, the LAD increased with the increase in the slope angle and TWI and was described by an exponential relationship. Otherwise, the statistical results of the landslides and the slope aspect showed that most of the landslide area was concentrated in the aspect of 110°~180° (SE to S). (3) The physically based susceptibility assessment results indicated that the prediction results were roughly consistent with the actual landslide distribution, and most areas with a high susceptibility were located on both sides of the river valley. The onset of heavy rain on 10 June 2019 was the main triggering factor of this group-occurring landslides. Our study will be beneficial for understanding the distribution pattern and cause of rainfall-induced shallow landslides in the Longchuan area, and it can provide data and technical support for the prevention of rainfall-induced geological disasters in the southeast mountainous area of China.

Author Contributions: Conceptualization, C.X. and S.M.; methodology, S.M.; software, S.M. and X.S.; validation, S.M. and X.S.; formal analysis, S.M. and X.S.; data curation, S.M. and X.S.; writing—original draft preparation, S.M.; writing—review and editing, C.X. and S.M.; supervision, C.X.; project administration, C.X.; funding acquisition, C.X. All authors have read and agreed to the published version of the manuscript.

Funding: This study was supported by the National Institute of Natural Hazards, Ministry of Emergency Management of China (ZDJ2020-10 and ZDJ2021-12).

Acknowledgments: We thank Google Earth and Sentinel-2 satellite images for the free access satellite images used in this study. We also express our appreciation of the constructive comments provided by the anonymous reviewers, which is beneficial for the quality of the manuscript a lot.

Conflicts of Interest: The authors declare that they have no known competing financial interests or personal relationships that could have appeared to influence he work reported in this paper.

References

1. Kirschbaum, D.; Kapnick, S.B.; Stanley, T.; Pascale, S. Changes in Extreme Precipitation and Landslides Over High Mountain Asia. *Geophys. Res. Lett.* **2020**, *47*, e2019GL085347. [CrossRef]
2. Emberson, R.; Kirschbaum, D.; Stanley, T. Global connections between El Nino and landslide impacts. *Nat. Commun.* **2021**, *12*, 2262. [CrossRef]
3. Petley, D. Global patterns of loss of life from landslides. *Geology* **2012**, *40*, 927–930. [CrossRef]
4. Lin, Q.; Wang, Y. Spatial and temporal analysis of a fatal landslide inventory in China from 1950 to 2016. *Landslides* **2018**, *15*, 2357–2372. [CrossRef]
5. Gariano, S.L.; Guzzetti, F. Landslides in a changing climate. *Earth Sci. Rev.* **2016**, *162*, 227–252. [CrossRef]
6. Huang, Y.; Xu, C.; Zhang, X.; Li, L. Bibliometric analysis of landslide research based on the WOS database. *Nat. Hazards Res.* **2022**, *2*, 49–61. [CrossRef]
7. Dai, L.; Scaringi, G.; Fan, X.; Yunus, A.P.; Liu-Zeng, J.; Xu, Q.; Huang, R. Coseismic Debris Remains in the Orogen Despite a Decade of Enhanced Landsliding. *Geophys. Res. Lett.* **2021**, *48*, e2021GL095850. [CrossRef]
8. Fan, X.; Yunus, A.P.; Scaringi, G.; Catani, F.; Siva Subramanian, S.; Huang, R. Rapidly Evolving Controls of Landslides After a Strong Earthquake and Implications for Hazard Assessments. *Geophys. Res. Lett.* **2020**, *48*, e2020GL090509. [CrossRef]
9. Fan, X.; Scaringi, G.; Korup, O.; West, A.J.; van Westen, C.J.; Tanyas, H.; Hovius, N.; Hales, T.C.; Jibson, R.W.; Allstadt, K.E.; et al. Earthquake-induced chains of geologic hazards: Patterns, mechanisms, and impacts. *Rev. Geophys.* **2019**, *57*, 421–503. [CrossRef]
10. Schmitt, R.; Tanyas, H.; Jessee, A.; Zhu, J.; Biegel, K.; Allstadt, K.; Jibson, R.; Thompson, E.; Westen, C.J.; Sato, H.; et al. *An Open Repository of Earthquake-Triggered Ground-Failure Inventories*; U.S. Geological Survey: Reston, VA, USA, 2017. [CrossRef]
11. Tian, Y.; Xu, C.; Yuan, R.-M. Earthquake-Triggered Landslides. *Treatise Geomorphol.* **2021**, *2*, 583–614. [CrossRef]
12. Xu, C.; Xu, X.; Zhou, B.; Shen, L. Probability of coseimic landslides: A new generation of earthquake-triggered landslide hazard model. *J. Eng. Geol.* **2019**, *27*, 1122. [CrossRef]
13. Shao, X.; Xu, C. Earthquake-induced landslides susceptibility assessment: A review of the state-of-the-art. *Nat. Hazards Res.* **2022**, in press. [CrossRef]
14. Kirschbaum, D.; Stanley, T. Satellite-Based Assessment of Rainfall-Triggered Landslide Hazard for Situational Awareness. *Earths Future* **2018**, *6*, 505–523. [CrossRef] [PubMed]
15. Emberson, R.; Kirschbaum, D.; Amatya, P.M.; Tanyas, H.; Marc, O. Insights from the topographic characteristics of a large global catalog of rainfall-induced landslide event inventories. *Nat. Hazards Earth Syst. Sci.* **2022**, *22*, 1129–1149. [CrossRef]
16. Marc, O.; Stumpf, A.; Malet, J.P.; Gosset, M.; Uchida, T.; Chiang, S.-H. Initial insights from a global database of rainfall-induced landslide inventories: The weak influence of slope and strong influence of total storm rainfall. *Earth Surf. Dyn.* **2018**, *6*, 903–922. [CrossRef]
17. Feng, W.; Bai, H.; Lan, B.; Wu, Y.; Wu, Z.; Yan, L.; Ma, X. Spatial–temporal distribution and failure mechanism of group-occurring landslides in Mibei village, Longchuan County, Guangdong, China. *Landslides* **2022**, *19*, 1957–1970. [CrossRef]
18. Ma, T.; Li, C.; Lu, Z.; Bao, Q. Rainfall intensity–duration thresholds for the initiation of landslides in Zhejiang Province, China. *Geomorphology* **2015**, *245*, 193–206. [CrossRef]
19. Chen, H.; Dadson, S.; Chi, Y.-G. Recent rainfall-induced landslides and debris flow in northern Taiwan. *Geomorphology* **2006**, *77*, 112–125. [CrossRef]
20. Merghadi, A.; Yunus, A.P.; Dou, J.; Whiteley, J.; ThaiPham, B.; Bui, D.T.; Avtar, R.; Abderrahmane, B. Machine learning methods for landslide susceptibility studies: A comparative overview of algorithm performance. *Earth Sci. Rev.* **2020**, *207*, 103225. [CrossRef]
21. Reichenbach, P.; Rossi, M.; Malamud, B.D.; Mihir, M.; Guzzetti, F. A review of statistically-based landslide susceptibility models. *Earth Sci. Rev.* **2018**, *180*, 60–91. [CrossRef]
22. Hong, H.; Pradhan, B.; Xu, C.; Tien Bui, D. Spatial prediction of landslide hazard at the Yihuang area (China) using two-class kernel logistic regression, alternating decision tree and support vector machines. *Catena* **2015**, *133*, 266–281. [CrossRef]
23. Shao, X.; Ma, S.; Xu, C.; Zhang, P.; Wen, B.; Tian, Y.; Zhou, Q.; Cui, Y. Planet Image-Based Inventorying and Machine Learning-Based Susceptibility Mapping for the Landslides Triggered by the 2018 Mw6.6 Tomakomai, Japan Earthquake. *Remote Sens.* **2019**, *11*, 978. [CrossRef]
24. Shao, X.; Ma, S.; Xu, C.; Zhou, Q. Effects of sampling intensity and non-slide/slide sample ratio on the occurrence probability of coseismic landslides. *Geomorphology* **2020**, *363*, 107222. [CrossRef]
25. Tanyu, B.F.; Abbaspour, A.; Alimohammadlou, Y.; Tecuci, G. Landslide susceptibility analyses using Random Forest, C4.5, and C5.0 with balanced and unbalanced datasets. *CATENA* **2021**, *203*, 105355. [CrossRef]
26. Kavzoglu, T.; Sahin, E.K.; Colkesen, I. An assessment of multivariate and bivariate approaches in landslide susceptibility mapping: A case study of Duzkoy district. *Nat. Hazards* **2015**, *76*, 471–496. [CrossRef]
27. Wang, Y.; Fang, Z.; Hong, H. Comparison of convolutional neural networks for landslide susceptibility mapping in Yanshan County, China. *Sci. Total Environ.* **2019**, *666*, 975–993. [CrossRef]
28. Xu, C.; Xu, X.; Dai, F.; Saraf, A.K. Comparison of different models for susceptibility mapping of earthquake triggered landslides related with the 2008 Wenchuan earthquake in China. *Comput. Geosci.* **2012**, *46*, 317–329. [CrossRef]

29. Arabameri, A.; Chandra Pal, S.; Rezaie, F.; Chakrabortty, R.; Saha, A.; Blaschke, T.; Di Napoli, M.; Ghorbanzadeh, O.; Thi Ngo, P.T. Decision tree based ensemble machine learning approaches for landslide susceptibility mapping. *Geocarto Int.* **2021**, *37*, 1–35. [CrossRef]
30. Adnan, M.S.G.; Rahman, M.S.; Ahmed, N.; Ahmed, B.; Rabbi, M.F.; Rahman, R.M. Improving Spatial Agreement in Machine Learning-Based Landslide Susceptibility Mapping. *Remote Sens.* **2020**, *12*, 3347. [CrossRef]
31. Rossi, M.; Guzzetti, F.; Reichenbach, P.; Mondini, A.C.; Peruccacci, S. Optimal landslide susceptibility zonation based on multiple forecasts. *Geomorphology* **2010**, *114*, 129–142. [CrossRef]
32. Ma, S.; Xu, C.; Shao, X. Spatial prediction strategy for landslides triggered by large earthquakes oriented to emergency response, mid-term resettlement and later reconstruction. *Int. J. Disaster Risk Reduct.* **2020**, *43*, 101362. [CrossRef]
33. Gutiérrez-Martín, A. A GIS-physically-based emergency methodology for predicting rainfall-induced shallow landslide zonation. *Geomorphology* **2020**, *359*, 107121. [CrossRef]
34. Hong, Y.; Adler, R.; Huffman, G. Evaluation of the potential of NASA multi-satellite precipitation analysis in global landslide hazard assessment. *Geophys. Res. Lett.* **2006**, *33*, L22402. [CrossRef]
35. Lin, Q.; Lima, P.; Steger, S.; Glade, T.; Jiang, T.; Zhang, J.; Liu, T.; Wang, Y. National-scale data-driven rainfall induced landslide susceptibility mapping for China by accounting for incomplete landslide data. *Geosci. Front.* **2021**, *12*, 101248. [CrossRef]
36. Iverson, R.M. Landslide triggering by rain infiltration. *Water Resour. Res.* **2000**, *36*, 1897–1910. [CrossRef]
37. Corominas, J.; van Westen, C.; Frattini, P.; Cascini, L.; Malet, J.P.; Fotopoulou, S.; Catani, F.; van Den Eeckhaut, M.; Mavrouli, O.; Agliardi, F.; et al. Recommendations for the quantitative analysis of landslide risk. *Bull. Eng. Geol. Environ.* **2014**, *73*, 209–263. [CrossRef]
38. Fell, R.; Corominas, J.; Bonnard, C.; Cascini, L.; Leroi, E.; Savage, W. Guidelines for landslide susceptibility, hazard and risk zoning for land use planning. *Eng. Geol.* **2008**, *102*. [CrossRef]
39. Sorbino, G.; Sica, C.; Cascini, L. Susceptibility analysis of shallow landslides source areas using physically based models. *Nat. Hazards* **2010**, *53*, 313–332. [CrossRef]
40. Baum, R.L.; Savage, W.Z.; Godt, J.W. *TRIGRS-A Fortran Program for Transient Rainfall Infiltration and Grid-Based Regional Slope-Stability Analysis, Version 2.0*; US Geological Survey: Reston, VA, USA, 2008; pp. 1159–2008.
41. Baum, R.L.; Godt, J.W.; Savage, W.Z. Estimating the timing and location of shallow rainfall-induced landslides using a model for transient, unsaturated infiltration. *J. Geophys. Res. F Earth Surf.* **2010**, *115*, F03013. [CrossRef]
42. Domènech, G.; Alvioli, M.; Corominas, J. Preparing first-time slope failures hazard maps: From pixel-based to slope unit-based. *Landslides* **2019**, *17*, 249–265. [CrossRef]
43. Schiliro, L.; Montrasio, L.; Scarascia Mugnozza, G. Prediction of shallow landslide occurrence: Validation of a physically-based approach through a real case study. *Sci. Total Environ.* **2016**, *569-570*, 134–144. [CrossRef] [PubMed]
44. Sarkar, S.; Roy, A.K.; Raha, P. Deterministic approach for susceptibility assessment of shallow debris slide in the Darjeeling Himalayas, India. *Catena* **2016**, *142*, 36–46. [CrossRef]
45. An, H.; Viet, T.T.; Lee, G.; Kim, Y.; Kim, M.; Noh, S.; Noh, J. Development of time-variant landslide-prediction software considering three-dimensional subsurface unsaturated flow. *Environ. Model. Softw.* **2016**, *85*, 172–183. [CrossRef]
46. Montrasio, L.; Valentino, R.; Losi, G.L. Rainfall-induced shallow landslides: A model for the triggering mechanism of some case studies in Northern Italy. *Landslides* **2009**, *6*, 241–251. [CrossRef]
47. Montrasio, L.; Valentino, R.; Corina, A.; Rossi, L.; Rudari, R. A prototype system for space–time assessment of rainfall-induced shallow landslides in Italy. *Nat. Hazards* **2014**, *74*, 1263–1290. [CrossRef]
48. Montrasio, L.; Valentino, R.; Meisina, C. Soil Saturation and Stability Analysis of a Test Site Slope Using the Shallow Landslide Instability Prediction (SLIP) Model. *Geotech. Geol. Eng.* **2018**, *36*, 2331–2342. [CrossRef]
49. Tran, T.V.; Lee, G.; An, H.; Kim, M. Comparing the performance of TRIGRS and TiVaSS in spatial and temporal prediction of rainfall-induced shallow landslides. *Environ. Earth Sci.* **2017**, *76*, 315. [CrossRef]
50. Escobar-Wolf, R.; Sanders, J.D.; Vishnu, C.L.; Oommen, T.; Sajinkumar, K.S. A GIS Tool for Infinite Slope Stability Analysis (GIS-TISSA). *Geosci. Front.* **2021**, *12*, 756–768. [CrossRef]
51. He, X.; Hong, Y.; Vergara, H.; Zhang, K.; Kirstetter, P.-E.; Gourley, J.J.; Zhang, Y.; Qiao, G.; Liu, C. Development of a coupled hydrological-geotechnical framework for rainfall-induced landslides prediction. *J. Hydrol.* **2016**, *543*, 395–405. [CrossRef]
52. Zhang, K.; Xue, X.; Hong, Y.; Gourley, J.J.; Lu, N.; Wan, Z.; Hong, Z.; Wooten, R. iCRESTRIGRS: A coupled modeling system for cascading flood–landslide disaster forecasting. *Hydrol. Earth Syst. Sci.* **2016**, *20*, 5035–5048. [CrossRef]
53. Rossi, G.; Catani, F.; Leoni, L.; Segoni, S.; Tofani, V. HIRESSS: A physically based slope stability simulator for HPC applications. *Nat. Hazards Earth Syst. Sci.* **2013**, *13*, 151–166. [CrossRef]
54. Tofani, V.; Bicocchi, G.; Rossi, G.; Segoni, S.; D'Ambrosio, M.; Casagli, N.; Catani, F. Soil characterization for shallow landslides modeling: A case study in the Northern Apennines (Central Italy). *Landslides* **2017**, *14*, 755–770. [CrossRef]
55. Salvatici, T.; Tofani, V.; Rossi, G.; D'Ambrosio, M.; Tacconi Stefanelli, C.; Masi, E.B.; Rosi, A.; Pazzi, V.; Vannocci, P.; Petrolo, M.; et al. Application of a physically based model to forecast shallow landslides at a regional scale. *Nat. Hazards Earth Syst. Sci.* **2018**, *18*, 1919–1935. [CrossRef]
56. Salciarini, D.; Fanelli, G.; Tamagnini, C. A probabilistic model for rainfall—induced shallow landslide prediction at the regional scale. *Landslides* **2017**, *14*, 1731–1746. [CrossRef]

57. Park, D.W.; Nikhil, N.V.; Lee, S.R. Landslide and debris flow susceptibility zonation using TRIGRS for the 2011 Seoul landslide event. *Nat. Hazards Earth Syst. Sci.* **2013**, *13*, 2833–2849. [CrossRef]
58. Liao, Z.; Hong, Y.; Kirschbaum, D.; Adler, R.F.; Gourley, J.J.; Wooten, R. Evaluation of TRIGRS (transient rainfall infiltration and grid-based regional slope-stability analysis)'s predictive skill for hurricane-triggered landslides: A case study in Macon County, North Carolina. *Natural Hazards* **2011**, *58*, 325–339. [CrossRef]
59. Lee, J.H.; Park, H.J. Assessment of shallow landslide susceptibility using the transient infiltration flow model and GIS-based probabilistic approach. *Landslides* **2015**, *13*, 885–903. [CrossRef]
60. Li, H.-C.; Wu, T.; Wei, H.-P.; Shih, H.-J.; Chao, Y.-C. Basinwide disaster loss assessments under extreme climate scenarios: A case study of the Kaoping River basin. *Nat. Hazards* **2016**, *86*, 1039–1058. [CrossRef]
61. Zhuang, J.; Peng, J.; Wang, G.; Iqbal, J.; Wang, Y.; Li, W.; Zhu, X. Prediction of rainfall-induced shallow landslides in the Loess Plateau, Yan'an, China, using the TRIGRS model. *Earth Surf. Processes Landf.* **2016**, *42*, 915–927. [CrossRef]
62. An, K.; Kim, S.; Chae, T.; Park, D. Developing an Accessible Landslide Susceptibility Model Using Open-Source Resources. *Sustainability* **2018**, *10*, 293. [CrossRef]
63. Hsu, Y.-C.; Liu, K.-F. Combining TRIGRS and DEBRIS-2D Models for the Simulation of a Rainfall Infiltration Induced Shallow Landslide and Subsequent Debris Flow. *Water* **2019**, *11*, 890. [CrossRef]
64. Saadatkhah, N.; Mansor, S.; Kassim, A.; Lee, L.M.; Saadatkhah, R.; Sobhanmanesh, A. Regional modeling of rainfall-induced landslides using TRIGRS model by incorporating plant cover effects: Case study in Hulu Kelang, Malaysia. *Environ. Earth Sci.* **2016**, *75*, 445. [CrossRef]
65. Gong, P.; Liu, H.; Zhang, M.; Li, C.; Wang, J.; Huang, H.; Clinton, N.; Ji, L.; Li, W.; Bai, Y.; et al. Stable classification with limited sample: Transferring a 30-m resolution sample set collected in 2015 to mapping 10-m resolution global land cover in 2017. *Sci. Bull.* **2019**, *64*, 370–373. [CrossRef]
66. Sato, H.; Harp, E. Interpretation of earthquake-induced landslides triggered by the 12 May 2008, M7.9 Wenchuan earthquake in the Beichuan area, Sichuan Province, China using satellite imagery and Google Earth. *Landslides* **2009**, *6*, 153–159. [CrossRef]
67. Tian, Y.; Owen, L.A.; Xu, C.; Ma, S.; Li, K.; Xu, X.; Figueiredo, P.M.; Kang, W.; Guo, P.; Wang, S.; et al. Landslide development within 3 years after the 2015 Mw 7.8 Gorkha earthquake, Nepal. *Landslides* **2020**, *17*, 1251–1267. [CrossRef]
68. Weidner, L.; Oommen, T.; Escobar-Wolf, R.; Sajinkumar, K.S.; Samuel, R.A. Regional-scale back-analysis using TRIGRS: An approach to advance landslide hazard modeling and prediction in sparse data regions. *Landslides* **2018**, *15*, 2343–2356. [CrossRef]
69. Tran, T.V.; Alvioli, M.; Lee, G.; An, H.U. Three-dimensional, time-dependent modeling of rainfall-induced landslides over a digital landscape: A case study. *Landslides* **2018**, *15*, 1071–1084. [CrossRef]
70. Alvioli, M.; Baum, R.L. Parallelization of the TRIGRS model for rainfall-induced landslides using the message passing interface. *Environ. Model. Softw.* **2016**, *81*, 122–135. [CrossRef]
71. Godt, J.; Baum, R.L.; Savage, W.Z.; Salciarini, D.; Schulz, W.; Harp, E.L. Transient deterministic shallow landslide modeling: Requirements for susceptibility and hazard assessments in a GIS framework. *Eng. Geol.* **2008**, *102*, 214–226. [CrossRef]
72. Ma, S.; Shao, X.; Xu, C.; He, X.; Zhang, P. MAT.TRIGRS (V1.0): A new open-source tool for predicting spatiotemporal distribution of rainfall-induced landslides. *Nat. Hazards Res.* **2021**, *1*, 161–170. [CrossRef]
73. Harp, E.; Michael, J.; Laprade, W. Shallow landslide hazard map of Seattle, Washington. *Rev. Eng. Geol.* **2008**, *20*, 67–82. [CrossRef]
74. Baumann, V.; Bonadonna, C.; Cuomo, S.; Moscariello, M.; Biass, S.; Pistolesi, M.; Gattuso, A. Mapping the susceptibility of rain-triggered lahars at Vulcano island (Italy) combining field characterization, geotechnical analysis, and numerical modelling. *Nat. Hazards Earth Syst. Sci.* **2019**, *19*, 2421–2449. [CrossRef]
75. Vieira, B.C.; Fernandes, N.F.; Augusto Filho, O.; Martins, T.D.; Montgomery, D.R. Assessing shallow landslide hazards using the TRIGRS and SHALSTAB models, Serra do Mar, Brazil. *Environ. Earth Sci.* **2018**, *77*, 260. [CrossRef]
76. Saulnier, G.-M.; Beven, K.; Obled, C. Including spatially variable soil depths in TOPMODEL. *J. Hydrol.* **1997**, *202*, 158–172. [CrossRef]
77. Bai, H.; Feng, W.; Yi, X.; Fang, H.; Wu, Y.; Deng, P.; Dai, H.; Hu, R. Group-occurring landslides and debris flows caused by the continuous heavy rainfall in June 2019 in Mibei Village, Longchuan County, Guangdong Province, China. *Nat. Hazards* **2021**, *108*, 3181–3201. [CrossRef]
78. Das, B. *Advanced Soil Mechanics*; Taylor & Francis: London, UK; New York, NY, USA, 2008.
79. He, J.; Qiu, H.; Qu, F.; Hu, S.; Yang, D.; Shen, Y.; Zhang, Y.; Sun, H.; Cao, M. Prediction of spatiotemporal stability and rainfall threshold of shallow landslides using the TRIGRS and Scoops3D models. *Catena* **2021**, *197*, 104999. [CrossRef]
80. Medina, V.; Hürlimann, M.; Guo, Z.; Lloret, A.; Vaunat, J. Fast physically-based model for rainfall-induced landslide susceptibility assessment at regional scale. *Catena* **2021**, *201*, 105213. [CrossRef]
81. Yu, C.-K.; Cheng, L.-W. Distribution and Mechanisms of Orographic Precipitation Associated with Typhoon Morakot (2009). *J. Atmos. Sci.* **2013**, *70*, 2894–2915. [CrossRef]
82. Liu, J.-K.; Shih, P.T.-Y. Topographic Correction of Wind-Driven Rainfall for Landslide Analysis in Central Taiwan with Validation from Aerial and Satellite Optical Images. *Remote Sens.* **2013**, *5*, 2571–2589. [CrossRef]
83. Chen, Y.-C.; Chang, K.-T.; Wang, S.F.; Huang, J.-C.; Yu, C.-K.; Tu, J.-Y.; Chu, H.-J.; Liu, C.-C. Controls of preferential orientation of earthquake- and rainfall-triggered landslides in Taiwan's orogenic mountain belt. *Earth Surf. Processes Landf.* **2019**, *44*, 1661–1674. [CrossRef]

84. Vorpahl, P.; Elsenbeer, H.; Märker, M.; Schröder, B. How can statistical models help to determine driving factors of landslides? *Ecol. Model.* **2012**, *239*, 27–39. [CrossRef]
85. Kavzoglu, T.; Sahin, E.K.; Colkesen, I. Landslide susceptibility mapping using GIS-based multi-criteria decision analysis, support vector machines, and logistic regression. *Landslides* **2014**, *11*, 425–439. [CrossRef]
86. Laimer, H.J. Anthropogenically induced landslides–A challenge for railway infrastructure in mountainous regions. *Eng. Geol.* **2017**, *222*, 92–101. [CrossRef]
87. Vuillez, C.; Tonini, M.; Sudmeier-Rieux, K.; Devkota, S.; Derron, M.-H.; Jaboyedoff, M. Land use changes, landslides and roads in the Phewa Watershed, Western Nepal from 1979 to 2016. *Appl. Geogr.* **2018**, *94*, 30–40. [CrossRef]
88. Li, Y.; Wang, X.; Mao, H. Influence of human activity on landslide susceptibility development in the Three Gorges area. *Nat. Hazards* **2020**, *104*, 2115–2151. [CrossRef]
89. Tanyaş, H.; Görüm, T.; Kirschbaum, D.; Lombardo, L. Could road constructions be more hazardous than an earthquake in terms of mass movement? *Nat. Hazards* **2022**, *112*, 639–663. [CrossRef]